

Token-Mol 1.0: tokenized drug design with large language model

Jike Wang^{1,#}, Rui Qin^{1,#}, Mingyang Wang^{1,#}, Meijing Fang¹, Yangyang Zhang¹, Yuchen Zhu¹, Qun Su¹, Qiaolin Gou¹, Chao Shen¹, Odin Zhang³, Zhenxing Wu¹, Dejun Jiang¹, Xujun Zhang¹, Huifeng Zhao¹, Xiaozhe Wan², Zhourui Wu, Liwei Liu^{2,*}, Yu Kang^{1,*}, Chang-Yu Hsieh^{1,*}, Tingjun Hou^{1,*}

¹*College of Pharmaceutical Sciences, Zhejiang University, Hangzhou 310058, Zhejiang, China*

²*Advanced Computing and Storage Laboratory, Central Research Institute, 2012 Laboratories. Huawei Technologies Co., Ltd., Nanjing 210000, Jiangsu, China*

³*Paul Allen School, University of Washington, Seattle*

⁴*Key Laboratory of Spine and Spinal cord Injury Repair and Regeneration, Ministry of Education, Tongji University, Shanghai, China;*

[#]*Equivalent authors*

Corresponding authors

Tingjun Hou

E-mail: tingjunhou@zju.edu.cn

Chang-Yu Hsieh

E-mail: kimhsieh@zju.edu.cn

Yu Kang

E-mail: yukang@zju.edu.cn

Liwei Liu

E-mail: liuliwei5@huawei.com

Abstract

Significant interests have recently risen in leveraging sequence-based large language models (LLMs) for drug design. However, most current applications of LLMs in drug discovery lack the ability to comprehend three-dimensional (3D) structures, thereby limiting their effectiveness in tasks that explicitly involve molecular conformations. In this study, we introduced Token-Mol, a token-only 3D drug design model. This model encodes all molecular information, including 2D and 3D structures, as well as molecular property data, into tokens, which transforms classification and regression tasks in drug discovery into probabilistic prediction problems, thereby enabling learning through a unified paradigm. Token-Mol is built on the transformer decoder architecture and trained using random causal masking techniques. Additionally, we proposed the Gaussian cross-entropy (GCE) loss function to overcome the challenges in regression tasks, significantly enhancing the capacity of LLMs to learn continuous numerical values. Through a combination of fine-tuning and reinforcement learning (RL), Token-Mol achieves performance comparable to or surpassing existing task-specific methods across various downstream tasks, including pocket-based molecular generation, conformation generation, and molecular property prediction. Compared to existing molecular pre-trained models, Token-Mol exhibits superior proficiency in handling a wider range of downstream tasks essential for drug design. Notably, our approach improves regression task accuracy by approximately 30% compared to similar token-only methods. Token-Mol overcomes the precision limitations of token-only models and has the potential to integrate seamlessly with general models such as ChatGPT, paving the way for the development of a universal artificial intelligence drug design model that facilitates rapid and high-quality drug design by experts.

Introduction

Drug discovery traverses a remarkably intricate journey. Recent years have witnessed profound advancements in artificial intelligence (AI) technologies, particularly deep learning (DL), which has been progressively permeating multiple facets of drug development. These technologies are emerging as critical catalysts for innovative drug research. However, the formidable cost associated with acquiring annotated data sets in drug discovery remains a significant impediment to the advancement in this field. Recently, the rapid evolution of unsupervised learning frameworks, epitomized by BERT¹ and GPT², has introduced unsupervised chemical and biological pre-training models across disciplines such as chemistry and biology³⁻¹⁶. These models undergo large-scale unsupervised training to learn representations of small molecules or proteins, subsequently fine-tuned for specific applications. This approach helps mitigate the challenges posed by sparse labeling and suboptimal out-of-distribution generalization, leading to improved performance¹⁷.

Large-scale molecular pre-training models can be broadly categorized into two main groups: models based on chemical language and models utilizing molecular graphs. Chemical language models, which encode molecular structures using representations such as simplified molecular input line entry system (SMILES)¹⁸ or self-referencing embedded strings (SELFIES)¹⁹, employ training methodologies akin to BERT or GPT, well-established in natural language processing (NLP). Notable examples include SMILES-BERT²⁰, MolGPT²¹, and Chemformer²², which exhibit architectural similarities to universal NLP models like ChatGPT, enabling smooth integration. However, a significant limitation of these string-based models is their inability to inherently process three-dimensional (3D) structural information that directly governs crucial physical, chemical, and biological properties of molecules. As a result, they are insufficient for downstream tasks involving 3D structures, such as molecular conformation generation and 3D structure-based drug design.

In contrast, graph-based molecular pre-trained models exhibit higher versatility. They represent molecules in a graphical format, with nodes for atoms and edges for

chemical bonds. Pre-training methodologies include various techniques, such as random masking of atom types, contrastive learning, and context prediction²³⁻²⁵. Unlike language-based models, graph-based molecular pre-trained models inherently incorporate geometric information, as demonstrated by methods like GEM²⁶ and Uni-Mol²⁷. However, these approaches primarily focus on learning molecular representations for property prediction, often overlooking tasks related to molecular design. Additionally, integrating them directly with universal NLP models is challenging. As of now, a general model for all drug design tasks remains elusive.

Nevertheless, the emergence of universal artificial intelligence opens up new avenues in this realm. Since the advent of ChatGPT, universal large language models have demonstrated impressive prowess in human-machine interactions, multi-turn dialogue comprehension, and reasoning. They assist in a wide array of tasks, ranging from email composition and translation to code generation. Furthermore, their applicability extends to fields such as mathematics, biophysics and chemistry. Recent studies reveal that GPT-4 showcases a profound understanding of key concepts in drug discovery, encompassing therapeutic proteins and fundamental principles governing the design of small molecule-based and other types of drugs. However, its effectiveness in specific drug design tasks, including *de novo* molecule generation, molecular structure alteration, drug-target interaction prediction, molecular property estimation, and retrosynthetic pathway prediction, necessitates enhancements²⁸. Although GPT-4's performance in drug design tasks requires further refinement, its token-only approach to handling continuous spatial data warrants attention. Building upon this concept, Born et al. introduced the Regression Transformer²⁹, which amalgamates regression tasks by encoding numerical values as tokens. Nevertheless, this method overlooks the intricate 3D structural complexities of molecules. Additionally, Flam-Shepherd and Aspuru-Guzik directly tokenize 3D atomic coordinates (XYZ) to represent molecular 3D structures³⁰. Both approaches have demonstrated promising results in relevant drug design tasks, highlighting the capacity of large models to grasp the semantics of numerical values and supporting the feasibility of using token-only models to handle continuous data.

However, directly training language models on Cartesian coordinates of atoms faces unique challenges. Specifically, for larger molecules, the extensive XYZ coordinates can generate excessively long sequences, hindering the model’s learning. Moreover, this approach fails to inherently address conformation invariance. Ganea et al. observed significant variations in torsion angles within molecules across different force fields, while atomic bond lengths and angles exhibit more rigidity³¹. Therefore, we prefer utilizing molecular SMILES representations and torsion angle tokens to represent 2D and 3D structures, framing all regression tasks as probabilistic prediction tasks.

Building upon the foundational principles outlined earlier, we introduce Token-Mol, a pioneering large-scale language model tailored for molecular pre-training. This model skillfully integrates crucial 3D structural information. Token-Mol is structured with a configuration comprising 12 layers of Transformer decoders, which undergo a rigorously designed pre-training regimen grounded in random causal masking. This pre-training framework is crafted to empower the model with both generative and representational learning capabilities, thereby enhancing its adaptability across a wide range of downstream tasks. To enhance the understanding of numerical data related to molecular configurations and properties, we propose the GCE loss function, a novel approach that departs from conventional methodologies. Furthermore, Token-Mol exhibits fine-tuning capacity tailored to specific tasks through reinforcement learning (RL).

To validate the capabilities of Token-Mol, we conducted comprehensive assessments spanning pocket-based molecular generation, molecular conformation generation and property prediction tasks. Experimental results reveal that in pocket-based molecular generation task, Token-Mol excelled in benchmarks and real-world drug design scenarios, generating molecules with enhanced Vina scores, higher quantitative estimates of drug-likeness (QED), and improved synthetic accessibility (SA) scores. Furthermore, in the molecular conformation generation task, Token-Mol surpasses existing existing state-of-the-art (SOTA) methods, achieving improvements of over 10% across various metrics, thus producing superior-quality conformations. For molecular property prediction, Token-Mol demonstrates performance on comparable to

SOTA methods in both classification and regression tasks.

Moreover, the integration of RL into Token-Mol further optimizes the performance of downstream tasks, an advantage over geometric GNN-based large models. For instance, we applied RL to refine the pocket-based molecular generation process, specifically targeting CDK2 and EGFR. This approach not only expedited the creation of molecules with enhanced activity but also ensured adherence to a broad range of physicochemical criteria, resulting in compounds that surpassed the performance of current reference molecules.

In conclusion, Token-Mol stands as a groundbreaking token-only 3D molecular language model. The aforementioned findings offer compelling evidence of the inherent potential in this framework, presenting a novel outlook on standardizing AI models for drug design.

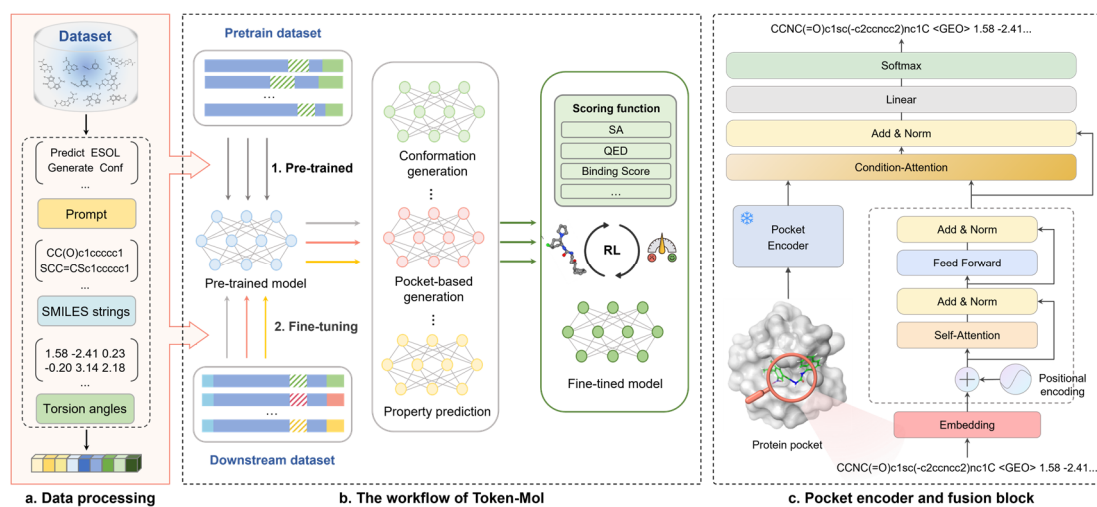


Fig. 1 | The overview of Token-Mol. (a) Data processing workflow. (b) The workflow of Token-Mol. (c) Pocket encoder and fusion block of pocket-based molecular generation.

Results

The overview of Token-Mol

The comprehensive workflow of Token-Mol is illustrated in **Fig. 1**. The initial phase involves pre-training on the dataset through random causal masking. Subsequently, the

model undergoes fine-tuning on customized datasets tailored to specific downstream tasks. For regression tasks, the GCE loss function is utilized during the fine-tuning process. Furthermore, the performance for specific downstream tasks can be further optimized using reinforcement learning.

The preprocessing of the pretraining dataset holds crucial significance in this context. As show in **Fig. 1a**, a depth-first search (DFS) traversal is conducted on the entire molecule in the standard SMILES format to extract the embedded torsion angles within the molecular structure. Following this, each extracted torsion angle is assimilated as a token appended to the SMILES string, with the “GEO” token serving as a delimiter between SMILES and torsion angle tokens. Throughout the pretraining phase, random causal masking based on causal regression is implemented. After pretraining, fine-tuning is carried out across downstream tasks. Notably, the highlighted yellow sections in the vector in **Fig. 1a** represent the task prompts designed for the construction of dialogue system, highlighting a key advantage of token-only models over other large-scale models: their capability to facilitate real-time interaction. At the end of the **Results** section, examples will be presented to illustrate this advantage.

Furthermore, for specific downstream tasks, we have developed specialized plugins. Notably, for the pocket-based molecular generation task, we introduced the pocket encoder and fusion block modules to seamlessly integrate protein and small molecule data. As depicted in **Fig. 1c**, we utilized a multi-head condition-attention mechanism to thoroughly incorporate information generated at each autoregressive step into subsequent iterations. This mechanism treats each token generated during autoregression as a prerequisite for further generation, thereby ensuring that the entire query, key, and value matrices originate from the original sequence.

However, in specialized applications such as pocket-based molecular design, the integration of receptor-ligand molecule pairs in the training dataset imposes inherent limitations. The model predominantly generates ligand molecules by utilizing information derived from the protein pocket. Consequently, the properties of these generated molecules are heavily influenced by the training data, restricting the explicitly control over their biophysical and chemical properties. These constraints are

particularly evident when a precise modulation of molecular properties is desired. In practical scenarios, a lead compound must satisfy numerous criteria, such as high bioactivity and favorable pharmacological properties, necessitating further optimizations. Token-Mol, built on an autoregressive language model architecture, where token generation aligns with actions in the RL framework, facilitates the seamless utilization of RL for optimization, thereby ensuring tailored outcomes.

To validate the performance of Token-Mol, we conducted comprehensive evaluations across three fundamental downstream tasks in drug design. Firstly, we assessed its effectiveness in pocket-based molecular design. Next, we evaluated its ability to generate high-quality molecular conformations. Finally, we examined its performance in predicting molecular properties.

Pocket-based molecular generation

In modern drug discovery, structure-based drug design holds paramount importance, driving researchers to rapidly identify high-affinity ligands within known protein binding pockets. Hence, pocket-based molecular generation, a method for generating potential ligands for specific pockets, not only avoids computationally intensive physical methods like molecular docking but also broadens the exploration of chemical space. Consequently, it serves as a crucial downstream task to demonstrate the effectiveness of our proposed model. Our goal is to generate ligand molecules tailored to specific protein pockets. To achieve this, as illustrated in **Fig. 1c**, we amalgamated a pocket encoder and a fusion block. We utilized a pretrained encoder to characterize protein pockets, ensuring its parameters frozen during fine-tuning. Furthermore, we employed condition-attention to integrate both protein and molecule information, mirroring a prompt-like mechanism that incorporates protein pocket information into the ligand molecule generation process. The additional methodological details are outlined in the **Methods** section.

We compared our model with several popular baseline models, including GraphBP³², Pocket2Mol³³, and TargetDiff³⁴. The first two models employ an

autoregressive generative graph neural network (GNN) architecture, while TargetDiff adopts a non-autoregressive, probabilistic diffusion model based on an SE(3)-equivariance network.

Performance on benchmark. Initially, we evaluated the generalization capability on pocket-based generation (without RL) by the following three criteria: fundamental attributes of the generated molecular sets, binding affinity towards a given pocket, and the physiochemical properties that indicate drug-likeness.

Table 1 | Properties of the reference and generated molecules by our model and other baseline models.

Metric	Token-Mol	GraphBP	Pocket2Mol	TargetDiff
Valid	0.973	0.830	1.000	0.972
IntDiv	0.849	0.879	0.812	0.860
Simi Ori.	0.132	0.051	0.097	0.107
Simi Training set	0.120	0.047	0.107	0.093
Higher Score	0.472	0.360	0.455	0.411

Valid: Validity of generated 3D structure, calculates as the proportion of 3D structures that can be translated into canonical SMILES; IntDiv: Internal diversity³⁵, an assessment of the distinctiveness of molecules within a molecular set, calculated using Tanimoto distance based on ECFP4 fingerprints^{36, 37}; Simi: Similarity between two molecular sets, calculate same as IntDiv. Higher score: the average ratio of Vina score of generated molecules exceeding the original molecule within each pocket. The bolded values represent the best performers in that metric.

As shown in **Table 1**, the molecules generated by Token-Mol exhibit superior performance across the entire molecular set. In terms of validity, graph-based models tend to generate some molecules with structural flaws, leading to a decreased validity³⁴. Our experiments partly confirm this issue in several graph-based models, excluding Pocket2mol. Although Token-Mol is a language model, inaccuracies in predicting token counts or values pertaining to torsion angles during autoregressive generation can yield invalid structures. Regarding internal diversity, Token-Mol demonstrates comparable performance to other models, highlighting its ability to explore chemical space under

specific pocket constraints.

As to pocket-based molecular generation, binding affinity is a crucial metric. Consistent with established practices, we employ the Vina score as the proxy measure of binding affinity. In terms of affinity, the performance of Token-Mol is approaching those of SOTA models specialized in pocket-based generation, which incorporate geometric deep learning principles. It also significantly outperforms the traditional GNN-based autoregressive generation model, GraphBP. Notably, 47.2% of Token-Mol's generated molecules exhibit superior binding affinity compared to the original molecules, outperforming all other models. Specifically, the median affinity (**Fig. 2, Table S1**) of the molecules generated by Token-Mol in the test set pockets exceeds those of the original molecules and the molecules generated by two expert models based on graph autoregression, GraphBP and Pocket2Mol, approaching the performance of the SOTA model TargetDiff.

In comparison with other models, Token-Mol (without RL) exhibits a Vina score distribution that closely aligns with the true distribution observed in the test set, indicating that its capability in accurately capturing the actual data distribution. Conversely, Pocket2Mol and TargetDiff generate molecules with notably broader Vina score distributions that deviate significantly from the test set distribution. Although these models can generate molecules with lower Vina scores, many of them are hallucinated, displaying low Vina scores but containing obvious structural anomalies that render them unsuitable as drug candidates in reality. These concerns are further explored in the section **Pocket-based generation on real-world targets**.

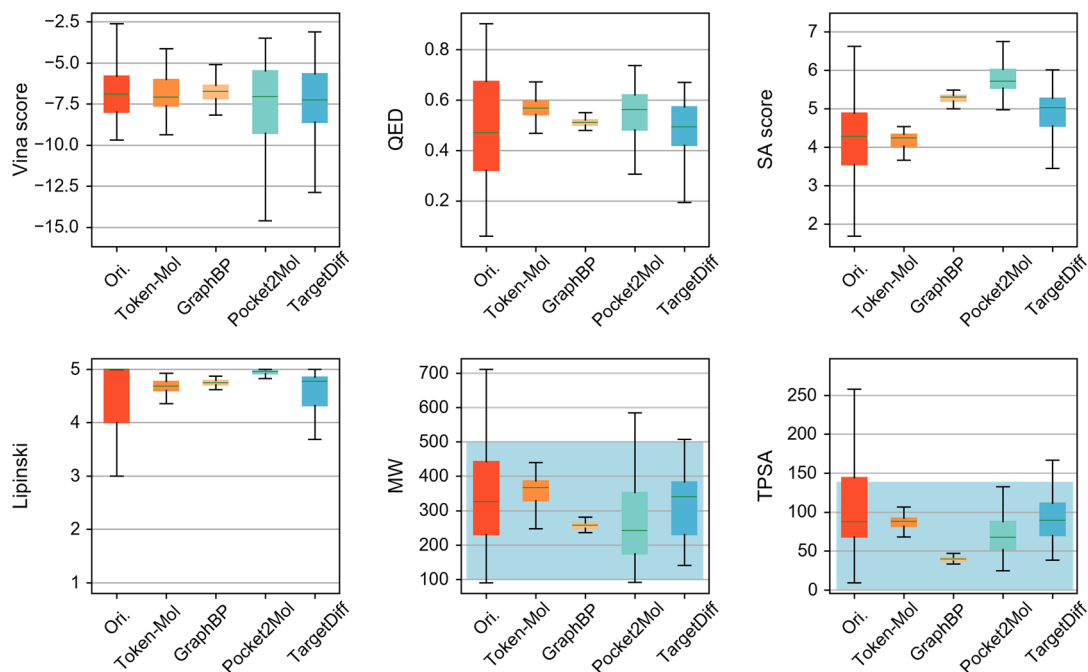


Fig. 2 | Comparison of the average molecular properties distribution in the test set pockets for the molecules from original test set or generated by Token-Mol and other baseline models. Vina score: the binding energy of ligands to protein pockets by using QVina2³⁸. QED: quantitative estimation of drug-likeness³⁹. SA score: synthetic accessibility score⁴⁰. Lipinski, the number that satisfies Lipinski's rule-of-five⁴¹. MW: molecular weights, the optimal range is between 100 and 600⁴². TPSA: topological polar surface area⁴³, the optimal range is between 0 and 140⁴⁴. The green bars stand for the median values, and the light blue shading represents the optimal range for that metric.

Physiochemical properties of molecules play a pivotal role in drug-likeness of drug candidates. In this regard, Token-Mol outperforms other models in generating molecules with better QED and SA Score, exceeding 5~10% benchmarks, thereby demonstrating its proficiency in creating more drug-like molecules. While Token-Mol slightly lags in Lipinski's rule metrics, its overall performance remains exceptional. Concerning molecular weight, Token-Mol's distribution aligns closely with the original molecules, staying within the optimal range, whereas GraphBP and Pocket2Mol have relatively lower median molecular weights, accounting for their ease in satisfying

Lipinski's rule. The metric TPSA determines the oral bioavailability and membrane permeability of molecules⁴⁴, with values below 140 Å² for cell membrane traversal and below 90 Å² for blood-brain barrier penetration. The TPSA distribution of molecules generated by Token-Mol falls within the range of 70-100 Å², which is more reasonable compared to other baseline models, suggesting superior absorption and potential for further drug discovery in central nervous system diseases⁴⁵.

Beyond metrics such as binding affinity and molecular properties, the fidelity of torsion angles within generated molecules needs to be considered. Our analysis involved the examination of torsion angles within the test set (**Fig. S1**). Subsequently, we curated a subset of torsion angles, characterized by their abundance and non-random distribution, enabling an in-depth comparative analysis. Jensen-Shannon divergence is used to assess the disparity between the torsion angle distributions in the test set and those of the molecules generated by the models (**Table 2**).

Table 2 | Jensen-Shannon divergence between the test set and molecules generated by Token-Mol and baseline models.

	Jensen-Shannon Divergence ($\times 10^{-1}$) ↓			
	Token-Mol	GraphBP	Pocket2Mol	TargetDiff
CNCC	0.240	N/A	1.749	1.637
C^CCC	0.281	N/A	1.385	1.496
CCCC	0.326	N/A	1.672	1.675
NCCC	0.421	N/A	2.269	1.767
NCC^C	0.427	N/A	2.173	1.644
COC^C	0.432	N/A	1.372	1.545
CCC=O	0.336	N/A	1.496	1.547
CNC=O	0.405	N/A	1.517	1.581
CNC^C	0.393	N/A	1.676	1.406

C [^] CC [^] C	0.552	N/A	1.397	N/A
Avg.	0.381	N/A	1.671	1.589

N/A means this type of torsion angle didn't appear in the molecules or is not detected due to the unreasonable conformation of the molecule. Symbol in the bond types: "=" represents double bond, "^" represents aromatic bond.

Furthermore, we calculated the average molecular generation time for each model. A faster generation speed indicates the ability to explore the chemical space under pocket constraints as much as possible in a limited timeframe, thereby accelerating the drug discovery process. This efficiency also reduces the demand for computational resources, enabling researchers with limited resources to effectively utilize the model.

To ensure a fair comparison, we measured the cumulative time spent by each model in sampling pockets and generating molecules until an output file (in sdf/mol2 format) was obtained. As shown in **Table 3**, Token-mol emerged as the fastest among the various models. When compared to models utilizing geometric deep learning frameworks, Token-Mol demonstrated a remarkably higher generation speed, averaging approximately 35 times faster for individual molecules. This efficiency stems from the different methodologies adopted by competing models. For instance, Pocket2Mol necessitates extensive sampling of molecular objects, excluding invalid or duplicate molecules to maintain diversity and validity. Similarly, TargetDiff requires performing thousands of rounds of sampling on the atoms within the pocket before molecule generation, ensuring high-quality outputs but significantly impeding the generation process for both models.

Furthermore, we evaluated the generation capabilities of the Token-Mol model on a cost-effective GeForce RTX4070 GPU with 12GB VRAM. The results indicate that the model can achieve a maximum batch size of 70, generating molecules within a given pocket at an average rate of 0.424s per molecule. This highlights the feasibility of deploying the model on consumer-grade computers for rapid inference.

Table 3 | Generation speed between different models on Tesla V100 GPU.

	Token-Mol	GraphBP	Pocket2Mol	TargetDiff
Times Spent (s/molecule)	0.365	0.750	13.103	12.971

Drug design for real-world targets. To evaluate the generalizability of models in designing drug candidates for real-world therapeutic targets, we selected 8 targets from three different protein families, including transferases, G-protein coupled receptors (GPCRs) and viral proteins, which had been widely studied in structure-based drug design⁴⁶⁻⁴⁸ and molecular generation⁴⁹⁻⁵². Specially, our selection includes a unique dimeric pocket from Programmed cell death 1 ligand 1 (PD-L1), aiming to explore the models’ capability in designing small-molecule modulators for protein-protein interactions.

To mimic a realistic drug discovery scenario, we generated an equal number of molecules across diverse targets, performed molecular docking, and calculated the molecular properties such as QED and SA Score for each molecule. Our goal was to produce “drug-like” molecules that possess high affinity to the target, excellent druglikeness, and favorable synthetic accessibility. To this end, we set criteria that a “drug-like” molecule should simultaneously satisfy a Vina Score of -8 kcal/mol or lower (equivalent to a dissociation constant K_d of approximately 1 μ M), a QED of at least 0.5, and an SA Score not exceeding 5.0.

As shown in **Table 4**, our approach achieved the highest ratio in six out of eight targets and the second-best result on the PD-L1 pocket. Specifically, For the targets including two transferases (CDK2 to DDR1) and two GPCRs (ARA2A and ADRB2), the Token-Mol model significantly outperformed other models, with 20%-30% of the generated molecules meeting our predefined criteria for “drug-like” molecules (except for DDR1). This performance is 2~3 times higher than the SOTA model TargetDiff. For the viral protein 3CLpro and the PD-L1 dimeric protein pocket, Token-Mol displayed comparable performance to other models, indicating its potential to generate reasonable molecules for real-world therapeutic pockets. Further analysis of the distributions of

Vina Scores and QED (**Figure S2, Table S1**) for the molecules generated by those models reveal that Token-Mol not only produces molecules with high affinity but also ensures they possess desirable properties. This aligns with the results for our test sets, suggesting that our model is capable of identifying promising lead compounds in real-world drug discovery scenarios.

Table 4 | The ratio of the “drug-like” molecules generated by each model for each target.

Target	Ideal molecules (%)			
	Token-Mol	GraphBP	Pocket2Mol	TargetDiff
CDK2	22.727	1.176	0	6.522
AKT1	17.241	0	0	2.174
EGFR	28.829	3.614	0	6.410
DDR1	6.481	0	0	5.128
ARA2A	30.909	2.353	7.339	18.947
ADRB2	34.259	1.136	4.255	5.495
3CLPro	0	0	0	0
PD-L1	24.074	2.174	27.434	6.849

Furthermore, we utilized cyclin-dependent kinases 2 (CDK2), representing kinases, and Adenosine A_{2A} Receptor (ARA2A), representing GPCR, as the examples from different protein families to further analyze the model’s capability in drug design for real-world targets. As shown in **Fig. 3**, the molecules generated by Token-Mol exhibit favorable drug-likeness, synthesizability, and promising affinity within the target pockets of two proteins that exhibit significant structural and functional differences. These molecules possess more rational structures compared to those generated by other models and display distinct scaffolds between the two different targets.

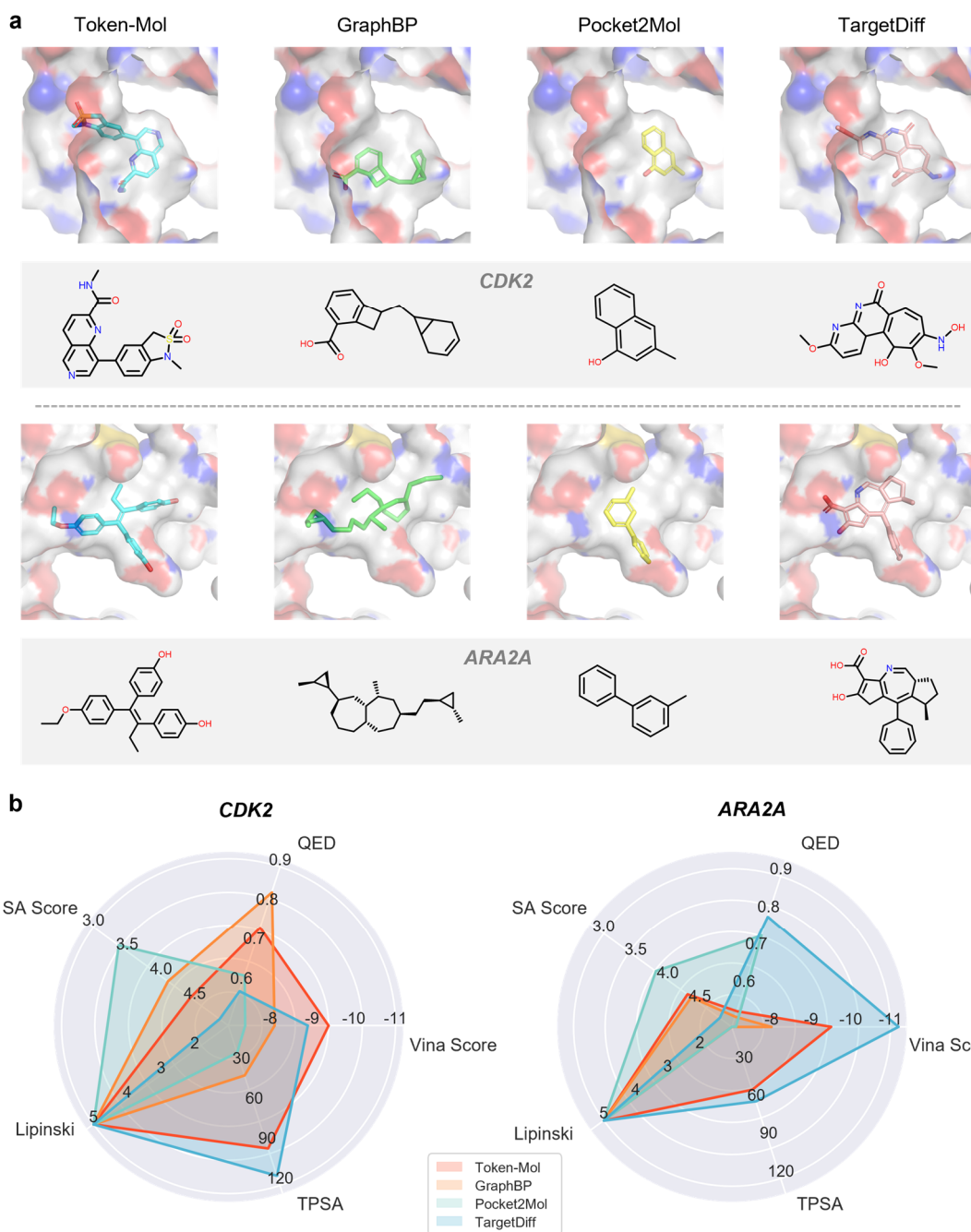


Fig. 3 | Evaluation on real-world targets. Comparison between (a) structures and binding modes, and (b) related molecular properties of “Drug-like” molecules with the highest affinity generated for CDK2 and ARA2A by the Token-Mol and baseline models. The detailed information of molecular properties is presented in **Table S3**.

Among the molecules generated by other baseline models, those produced by GraphBP exhibit distorted conformations, while those by Pocket2Mol are simple aromatic ring derivatives and exhibit minimal differences between the two targets.

Similar phenomena can also be observed in the molecules generated by the aforementioned two models in other use cases (Figure S4). As for the molecules generated by TargetDiff, while they demonstrate favorable results in terms of QED and Vina score, it is noteworthy that molecules for two targets contain tricyclic scaffolds and 7-membered cyclic groups, which are challenging to synthesis. This can explain why the molecules generated by TargetDiff have higher Vina scores in the former test, as these groups with large volume occupy as much space as possible within the pocket, creating more hydrophobic contacts. The predicted binding modes further confirm this, as the molecules generated by Token-Mol fit the shape of the pocket cavity more precisely, whereas those generated by other baseline models only occupy part of the pocket cavity.

To further demonstrate Token-Mol's capability to generate molecules that resemble real-world ligands, we chose ARA2A as the target to analyze the similarity between ligands and generated molecules. We selected several molecules from Token-Mol and TargetDiff that exceeded the average Vina score and QED thresholds of reference molecules against ARA2A (**Table S5**) for display. In **Fig. 4**, we present six real ligands of ARA2A, including agonists and antagonists. Notably, adenosine, the leftmost ligand, serves as the natural ligand of ARA2A and contains a purine scaffold. The other discovered ARA2A ligands all possess a nitrogen heterocyclic core as their scaffold, similar to purine, which can be monocyclic, bicyclic, or tricyclic⁵³. From the perspective of medicinal chemists, for the antagonists, which are majority of ARA2A ligands, their structure-activity relationship (SAR) and co-crystallized structures indicate that, in addition to the nitrogen heterocyclic scaffold, there are aromatic rings such as furan, thiophene, or benzene directly connected to the scaffold or located one or two carbon atoms away from it⁵⁴. These aromatic groups can fit into the internal space of the target pocket and engage in π - π stacking interactions⁵⁵, thereby enhancing the ligand's affinity for the receptor and enabling strong competition with the natural ligand.

Among the molecules generated by Token-Mol, it can be observed that most contain monocyclic or bicyclic nitrogen heterocyclic scaffolds resembling real-world

ligands, whereas those generated by TargetDiff differ significantly from real-world ligands. Furthermore, these molecules with nitrogen heterocyclic scaffolds possess aromatic rings, such as benzene or pyrazole, directly connected to the scaffold, consistent with the aforementioned SAR. This suggests that these molecules may conform to the SAR of ARA2A antagonists and exhibit good affinity for the target.

Simultaneously, we calculated the similarity of Bemis-Murcko scaffold⁵⁶ and Fréchet ChemNet Distance⁵⁷ (FCD) between the molecules generated by Token-Mol and other baseline models and the reference molecules (**Table S4**). The results demonstrate that Token-Mol generates molecules with higher similarity to the real-world ligands across all tested targets compared to other baseline models. Importantly, this similarity remains within an acceptable range to ensure molecular novelty, further supporting our conclusion that Token-Mol can generate molecules that closely resemble real-world ligands.

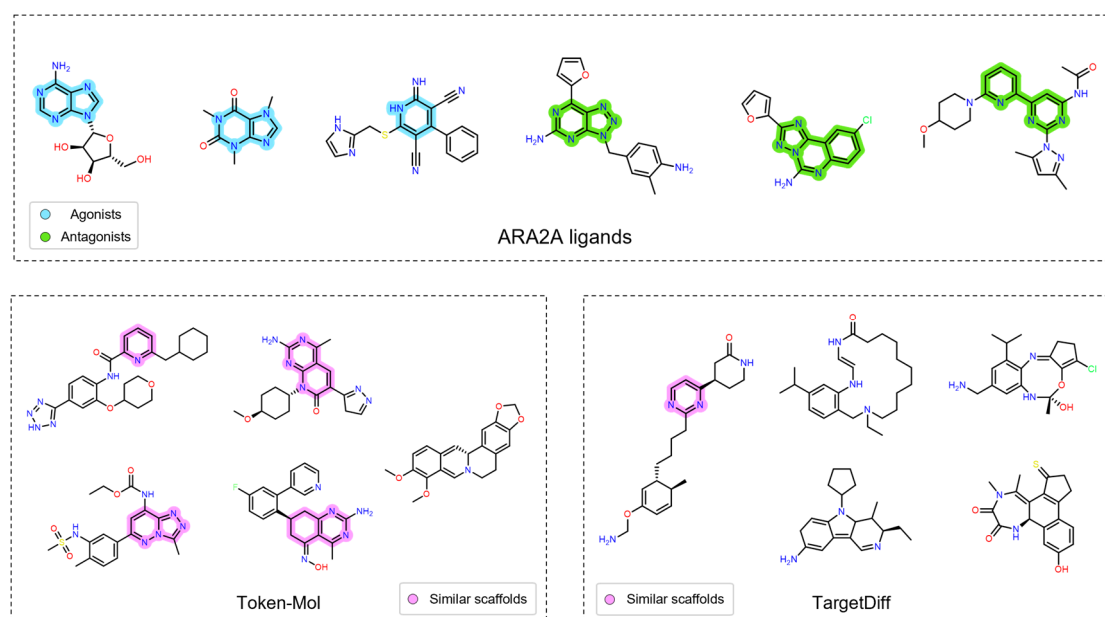


Fig. 4 | Comparison between the real-world ligands of ARA2A and molecules generated by Token-Mol and TargetDiff. The scaffolds of the real-world ARA2A ligands and those of molecules similar to the real-world ligands generated by the models are highlighted.

Further optimization with reinforcement learning. The content above has already demonstrated that Token-Mol can generate molecules with high drug-likeness, ease of

synthesis, and rational structures in the pockets of given targets. However, when compared to the state-of-the-art expert models like TargetDiff for pocket-aware generation, the molecules generated by Token-Mol still exhibit lower affinity to pockets from the test set and selected real-world targets (**Tables S1 and S2**). To address this, we have introduced a reinforcement learning approach to optimize the affinity of generated molecules for specific target pockets. Within this framework, constraints such as conformational clash and drug-likeness are enforced to ensure that the molecules maintain desirable properties. This strategy aims to maximize affinity for target pockets while preserving the excellent molecular properties demonstrated by the model, as detailed in the **Methods** section. Notably, optimizing geometric graph-based models such as TargetDiff is challenging due to their high complexity, and RL has not yet been applied to these models for 3D pocket-based molecular generation.

We conducted a total of 1,000 steps of reinforcement learning optimization on CDK2 and ARA2A, the two targets used for demonstration in the previous section. Throughout the reinforcement learning process, we recorded the average values of key metrics at each step (**Fig. 5a**). It can be observed that during the training of the two targets, the reward score essentially converged within 1,000 steps, indicating the stabilization of the agent model's training. Regarding our primary optimization objective, the Vina score, the average value is optimized from around -8 to approximately -9.5, with no significant oscillations observed after convergence. As for QED, which serves as a constraint condition, although the reward term in the reward function is binary rather than positively correlated with QED, it was found that the QED value initially increased and then converged as the reinforcement learning steps increased for both targets, suggesting that QED is also optimized under the set reward function. Although different trends were observed in the SA score during the reinforcement learning process for the two targets, the results remained below the threshold of 5, consistent with our previous tests (**Fig. S4**) that focused solely on affinity optimization. These trends demonstrate that our model can achieve optimization in molecule generation tasks for specific target pockets through reinforcement learning under constraints.

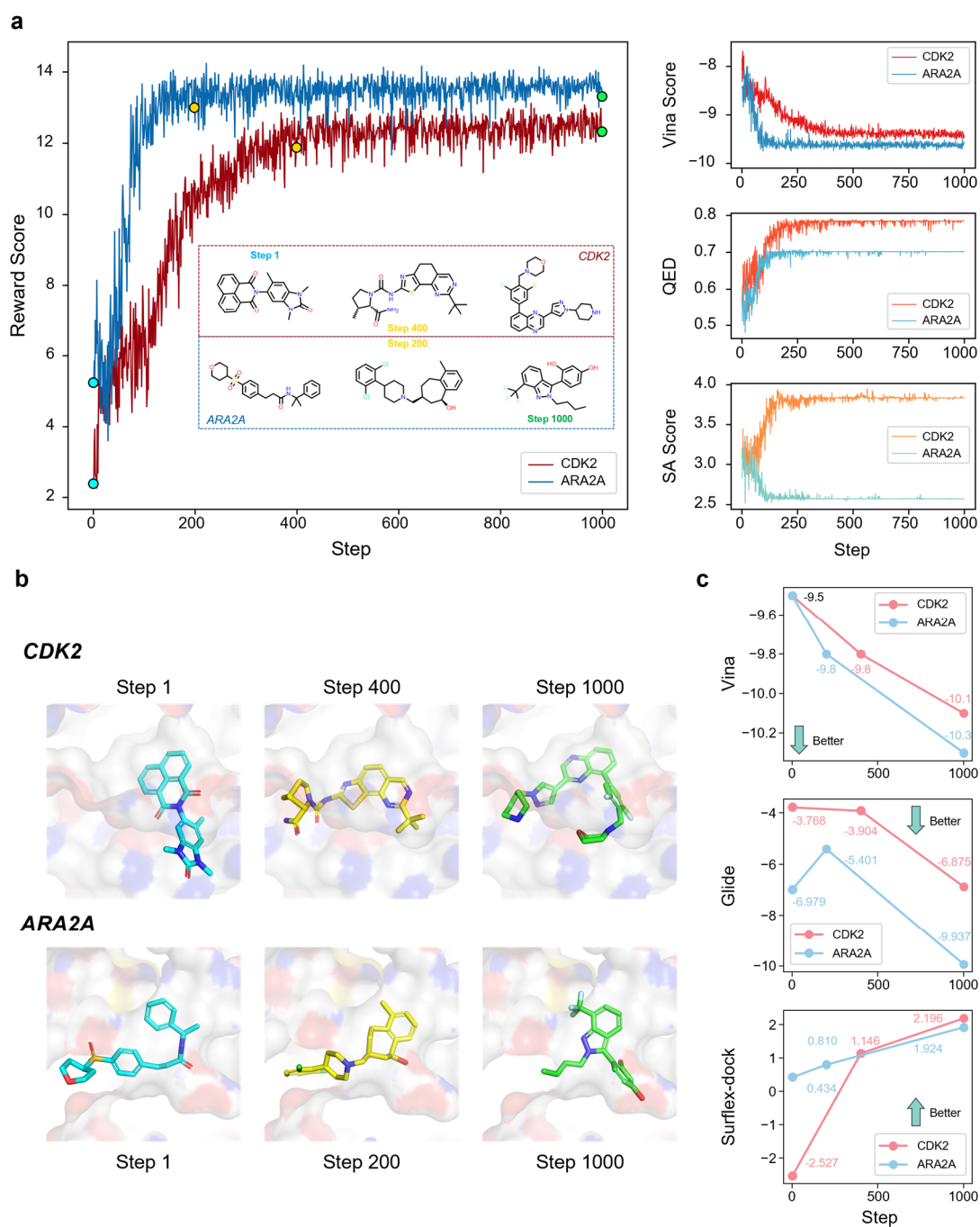


Fig. 5 | Molecular performance in RL process. (a) Key metrics such as reward score, Vina score, QED and SA score during the process of RL. The 2D structure of molecules from the different stages in the RL are also displayed. (b) The binding modes of selected molecules predicted with QVina2. (c) Change trends in the predicted affinities of these molecules for their respective targets using different docking methods.

Additionally, we selected molecules from the first step, the last step, and step before

the convergence of the reward score, showcasing the molecule with the highest affinity in those steps (**Fig. 5a**). From the perspective of specific molecules, it is obvious that the molecular scaffolds undergo substantial changes at different training stages, and the occurrence of unreasonable structures such as tricyclic structures or seven-membered ring groups also decreases. For their binding modes (**Fig. 5b**), it can be seen that the scaffold gradually fits into the pocket, which explains the gradual improvement of the Vina score during the training process.

Furthermore, to reduce the bias introduced by a single docking method, we conducted additional docking tests using Glide⁵⁸ and Surflex-dock⁵⁹ for the molecules presented in **Fig. 5c**, and the results demonstrate that reinforcement learning indeed optimized the molecules' affinity for the targets. In the case of CDK2, the docking scores (i.e., the predicted affinities) obtained from all three methods improved as the training steps increased. In ARA2A, a similar trend was observed, with the exception of Glide. Overall, in both targets, the molecules obtained after training convergence achieved the best results across all three docking methods, further confirming the capability of reinforcement learning to optimize the affinity of generated molecules for the target pockets.

Molecular Conformation Generation

Molecular conformation is a pivotal determinant of the chemical, physical, and biological properties of molecules, highlighting its fundamental role in drug design. Conformational generation is essential in this context, as it reveals the diverse spatial arrangements a molecule can adopt, which is critical for understanding its interactions with biological targets. This approach facilitates the identification of optimal conformations for target binding, thereby enhancing the drug's efficacy and selectivity. Additionally, exploring various conformations aids in elucidating their impact on biological activity, which is instrumental in developing more potent drugs. In virtual screening, conformational generation ensures comprehensive consideration of all potential molecular shapes, thereby increasing the likelihood of discovering promising drug candidates. This process is also crucial for predicting the drug's absorption,

distribution, metabolism, excretion, and toxicity (ADMET) properties, ultimately leading to the development of safer and more effective therapeutics. Furthermore, it provides critical insights into the interactions between different conformations and mutated targets, facilitating the design of drugs capable of circumventing resistance mechanisms.

Traditional methods for obtaining precise molecular conformations, such as X-ray crystallography and density functional theory (DFT), are either costly or computationally intensive, rendering them impractical for large-scale dataset analysis. The advent of deep geometric learning has introduced alternative methodologies for generating molecular conformations^{30, 60-66}.

In this study, we benchmarked our proposed approach against established baselines using widely recognized conformation generation benchmarks. We employed the dataset utilized by Zhang et al., which includes the dataset from Shi et al. (test set I) comprising 200 molecules, each with fewer than 100 conformations. On the other hand, the GEOM-Drug dataset presents a broader range of conformation counts per molecule, from 0 to 12,000. To address this variance, Zhang et al. introduced test set II²⁶, consisting of 1,000 randomly selected molecules with conformation counts distributed similarly to the entire dataset, ranging from 0 to 500.

Our evaluation metrics include both Recall and Precision. Recall measures the diversity of the generated conformations, while Precision evaluates the rationality of the generated conformations. We calculated the mean scores of coverage (COV) and matching (MAT) for both Recall and Precision. COV quantifies the extent to which the quantum computation conformation set covers the generated conformation set within a specified RMSD threshold, with higher values indicating better coverage. Conversely, MAT assesses the similarity between the generated conformations and the quantum mechanical-level training conformations, with lower values suggesting better performance.

Table 5 presents the results for test set I, indicating that Token-Mol’s generated conformations exhibit slightly lower Recall performance compared to GeoDiff and Tora3D, positioning it as the second-highest performer overall. This suggests that

Token-Mol’s conformation generation demonstrates diversity comparable to existing SOTA methodologies. However, Token-Mol surpasses other SOTA methods in both Precision metrics, resulting in substantial advantages. Notably, Token-Mol achieves significant superiority in the COV-P metric, outperforming Tora3D by approximately 11%, underscoring the superior quality of molecules produced by Token-Mol relative to alternative methods.

The findings for test set II, depicted in **Table 6**, reveal Token-Mol’s exemplary performance across all assessment metrics. Remarkably, Token-Mol attains the highest performance in both Precision-based evaluation metrics, COV-P and MAT-P, surpassing other models by approximately 24% and 21%, respectively.

Table 5 | Performance comparison of models on test set I.

Model	COV-R (%) \uparrow	MAT-R (\AA) \downarrow	COV-P (%) \uparrow	MAT-P (\AA) \downarrow
CGVAE	0.00	3.0702	-	-
GraphDG	8.27	1.9722	2.08	2.4340
CGCF	53.96	1.248	21.68	1.8571
ConfVAE	55.20	1.2380	22.96	1.8287
GeoMol	67.16	1.0875	-	-
ConfGF	62.15	1.1629	23.42	1.7219
GeoDiff	82.96 ★	0.9525	48.27	1.3205
Tora3D	80.37	0.9272 ★	62.22☆	1.1524☆
Token-Mol	80.65☆	0.9488☆	69.20 ★	1.0865 ★

★ represents the best, ☆ represents the second best.

Table 6 | Performance comparison of models on test set II.

nRotb	Model	COV-R (%) \uparrow	MAT-R (\AA) \downarrow	COV-P (%) \uparrow	MAT-P (\AA) \downarrow
	CGVAE	40.06	1.3771	-	-
All nRotb	GeoMol	72.50	1.1000	61.15	1.2009
	Tora3D	81.92	0.9297	62.16	1.1600

	Token-Mol	82.34	0.8936	76.87	0.9107
nRotb \leq 10	CGVAE	42.43	1.3296	-	-
	GeoMol	76.36	0.9380	57.29	1.1611
	Tora3D	83.03	0.8704	63.81	1.0906
	Token-Mol	83.25	0.8404	78.96	0.8108
nRotb $>$ 10	Tora3D	57.23	1.2455	29.02	1.5583
	Token-Mol	65.09	1.1257	47.52	1.3670

Subsequently, we investigated the relationship between the benchmark performance and the number of rotatable bonds, as illustrated in Fig. 6. Our analysis reveals a clear trend: the performance across all assessment metrics declines as the number of rotatable bonds increases. This decline becomes particularly pronounced when the number of rotatable bonds exceeds 10. Notably, Tora3D exhibits a significant drop in performance when generating conformations for molecules with a higher number of rotatable bonds. In contrast, Token-Mol demonstrates substantial advantages under these conditions.

Moreover, Token-Mol demonstrates impressive speed. During our evaluation on test set I, utilizing the Tesla V100 for the generation process, Token-Mol required an average of 6.37 seconds to generate all conformations for a single molecule, compared to 8.78 seconds per molecule for Tora3D.

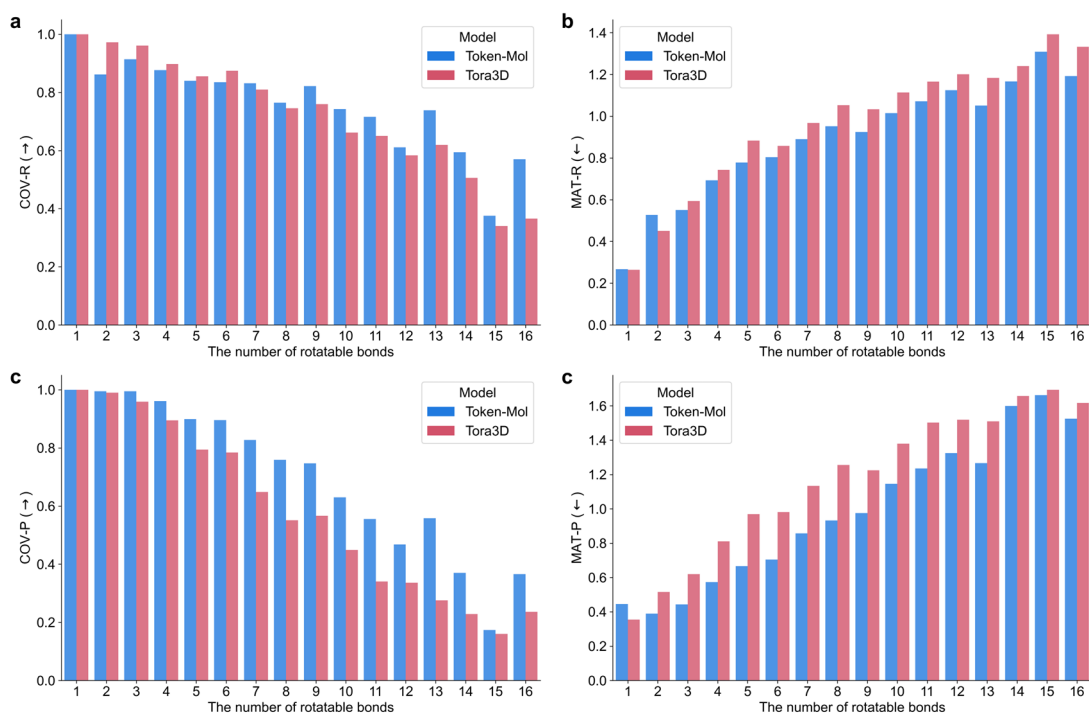


Fig. 6 | Performance for different number of rotatable bonds on test set II. The x-axis represents the number of rotatable bonds, and the y-axis indicates the prediction performance. **(a)** COV-R, **(b)** MAT-R, **(c)** COV-P and **(d)** MAT-P.

Molecular property prediction

Molecular representation is fundamental to molecular design, as it critically influences the execution of downstream tasks. In this study, we initially assessed the molecular representation capabilities of Token-Mol in the context of molecular property prediction.

Classification task. For the classification task, we selected six commonly used classification datasets and compared Token-Mol against five representative baselines: XGBoost⁶⁷ (conventional machine learning), K-Bert⁶⁸ (sequence-based model), Chemprop⁶⁹ (graph neural networks), GEM²⁶ (geometry-enhanced graph neural networks), and MapLight+GNN⁷⁰ (an integrated model combining traditional machine learning with graph neural networks). As outlined in **Table 7**, Token-Mol demonstrates noteworthy performance across all datasets, outperforming XGBoost and Chemprop in terms of accuracy, albeit marginally trailing behind MapLight+GNN and GEM. Notably, Token-Mol achieves state-of-the-art proficiency on single-task-focused

datasets such as BBBP and BACE.

Table 7 | Performance on different dataset for classification tasks.

Classification (ROC-AUC %↑)							
DataSets	BBBP	BACE	ClinTox	Tox21	ToxCast	SIDER	Average
#Moleculars	2039	1513	1478	7831	8575	1427	-
#Tasks	1	1	2	12	617	27	-
XGBoost	0.888 \pm	0.872 \pm	0.863 \pm	0.801 \pm	0.668 \pm	0.652 \pm	0.791
	0.028	0.016	0.034	0.061	0.164	0.086	
Chemprop	0.927 \pm	0.865 \pm	0.877 \pm	0.845 \pm	0.736 \pm	0.639 \pm	0.815
	0.021	0.037	0.037	0.015	0.005	0.028	
MapLight+GNN	0.912 \pm	0.883 \pm	0.895 \pm	0.865\pm	0.771 \pm	0.695\pm	0.836
	0.026	0.007	0.041	0.067	0.156	0.051	
GEM	0.940 \pm	0.898 \pm	0.940 \pm	0.862 \pm	0.766 \pm	0.670 \pm	0.846
	0.022	0.019	0.026	0.014	0.009	0.012	
K-Bert	0.945 \pm	0.879 \pm	0.913 \pm	0.665 \pm	0.510 \pm	0.608 \pm	0.757
	0.008	0.028	0.046	0.004	0.003	0.012	
Token-Mol	0.934 \pm	0.896 \pm	0.927 \pm	0.829 \pm	0.746 \pm	0.644 \pm	0.829
	0.001	0.015	0.021	0.005	0.012	0.020	

Regression task. We employed a set of six regression datasets for a thorough comparison and analysis. To extend beyond established benchmarks, we introduced the token-only Regression Transformer (RT)²⁹, a model conceptually akin to Token-Mol, to enrich our evaluation framework. Both RT and Token-Mol fully tokenize the input and output, enabling seamless integration with foundational large models, a feature not shared by other models.

A key advantage of token-only models over traditional regression models is their ability to interface seamlessly with large models such as ChatGPT, enabling real-time interaction. However, previous models like RT have shown suboptimal performance in

prediction tasks, limiting their utility for high-quality interactions. In contrast, Token-Mol treats each numerical value as a single token, rather than decomposing them into multiple tokens like RT. This approach enables one-shot prediction, thereby accelerating the prediction process. Combined with the GCE, Token-Mol achieves high-quality prediction results. These methodology allows Token-Mol to perform faster and deliver higher prediction quality.

As illustrated in **Table 8**, Token-Mol’s superiority in regression tasks is evident, outperforming established benchmarks such as XGBoost, K-Bert, and token-only RT. Notably, Token-Mol consistently surpasses RT across all tasks, showcasing an average performance enhancement of approximately 30%. Particularly remarkable is Token-Mol’s substantial performance boost on the Aqsol dataset, achieving an improvement of around 50%. Additionally, as depicted in Table 8, Token-Mol’s performance closely mirrors that of graph neural network-based models on datasets with large amounts of data, such as Aqsol, LD50, and Lipophilicity. These results collectively underscore the significant potential of Token-Mol in property prediction tasks.

Table 8 | Performance on different dataset for regression tasks.

Regression (RMSE ↓)							
DataSets	ESOL	FreeSolv	Lipo	Caco2	LD50	Aqsol	Average
#Moleculars	1128	642	4200	906	7385	9982	-
XGBoost	1.112 ±	1.958 ±	0.909 ±	0.455 ±	0.651 ±	1.540 ±	1.104
	0.086	0.245	0.032	0.031	0.024	0.017	
Chemprop	0.549 ±	1.106 ±	0.603 ±	0.429 ±	0.600 ±	1.000 ±	0.715
	0.028	0.125	0.020	0.019	0.021	0.038	
MapLight+GNN	0.529 ±	0.959 ±	0.623 ±	0.352 ±	0.600 ±	1.023 ±	0.681
	0.062	0.278	0.018	0.016	0.032	0.031	
GEM	0.543 ±	0.976 ±	0.584 ±	0.345 ±	0.576 ±	0.964 ±	0.665
	0.041	0.140	0.030	0.038	0.015	0.033	
K-Bert	0.671 ±	1.026 ±	0.641 ±	0.377 ±	0.596 ±	1.102 ±	0.736

	0.086	0.077	0.011	0.022	0.043	0.025	
RT	0.657 ±	1.389 ±	1.046 ±	0.483 ±	0.698 ±	2.344 ±	1.103
	0.031	0.235	0.528	0.049	0.055	0.630	
Token-Mol	0.722 ±	1.468 ±	0.670 ±	0.441 ±	0.644 ±	1.237 ±	0.864
(w/o GCE)*	0.022	0.220	0.028	0.048	0.025	0.050	
Token-Mol	0.593 ±	1.225 ±	0.645 ±	0.399 ±	0.611 ±	1.157 ±	0.772
	0.036	0.211	0.026	0.010	0.038	0.064	

*Token-Mol (w/o GCE) is the model without GCE.

The efficiency of GCE. Token-only generative models conventionally employ cross-entropy loss for regression tasks, but they often exhibit insensitivity to numerical values and fail to capture the relationships between them. To address this issue, we proposed the GCE loss function for regression-related downstream tasks in molecular property prediction. To assess the efficacy of GCE, we conducted ablation experiments to compare models with and without GCE (**Table 8**). Our results indicate that the absence of GCE significantly impairs Token-Mol’s performance across all datasets, with an average RMSE increase of approximately 12%, underscoring the critical role of GCE in regression tasks. Compared to RT, which decomposes individual numerical values into multiple token representations, Token-Mol’s one-shot approach, enhanced with GCE, demonstrates substantial improvements in both prediction accuracy and efficiency.

Despite the significant improvements demonstrated by Token-Mol compared to RT, it still exhibits certain limitations relative to other large models based on GNN. This discrepancy is primarily due to the model’s insufficient sensitivity to numerical values. Although we proposed the GCE loss function to address this issue, Token-Mol still lags behind graph neural network-based regression models. Future work will focus on enhancing the model’s performance in regression tasks through approaches such as multi-task prediction and data augmentation.

Chat to Token-Mol

Token-Mol exhibits significant potential compared to existing pre-trained large models, particularly in its ability to integrate seamlessly with general-purpose large models and facilitate unrestricted dialogue. This integration leverages techniques from various large language models, including prompt learning, mixture of experts (MoE)⁷¹, and retrieval-augmented generation (RAG)⁷².

To illustrate this capability, we present several straightforward dialogue use cases. By employing prompt learning, we can control the execution of tasks such as property prediction mentioned in this study. Initially, we insert specific prompts, such as “Predict ESOL” to fine-tune the model. As shown in **Fig. S7**, this enables direct interaction with the model post-prompting, allowing users to request predictions of different molecular properties. In this example, we queried various properties of different molecules, and Token-Mol successfully provided the corresponding predictions. This demonstrates potential of Token-Mol for engaging in meaningful dialogues with chemists. Users may provide molecular conformations, but since Token-Mol can generate the corresponding conformations, the final output will include only the predicted target properties.

Additionally, future iterations can incorporate RAG. When querying Token-Mol about a specific property of a molecule, the system employs vector search based on embeddings to convert the query into a vector. This vector is then matched with highly relevant vector descriptions from a database to provide contextual information. The query, along with the retrieved context such as spatial structure information and other relevant properties, is then input to Token-Mol, which then generates the answer.

The aforementioned example highlights the unique of token-only models to seamlessly integrate with general models, a capability that is not exhibited by other types of models.

Discussion

This study proposes Token-Mol, the inaugural token-only extensive pre-trained language model tailored for drug design. Rooted in the GPT framework, Token-Mol

integrates random causal masking to enhance its flexible applicability across diverse drug design tasks. Additionally, we propose the Gaussian cross-entropy loss function to foster improved acquisition of continuous spatial information throughout model training, thereby notably reinforcing its performance in regression tasks. Furthermore, through the integration of RL, Token-Mol achieves expedited optimization towards predetermined objectives in specific tasks, aiming to achieve desired outcomes efficiently. To substantiate these capabilities, we conducted assessments across three pivotal drug design tasks.

In pocket-based generation task, Token-Mol achieve results close to expert models in the pocket-based generation task and obtain optimal results in terms of drug-likeness and synthesizability of molecules. Benefit from the rapid inference of the language model, Token-Mol can generate molecules within the pocket in a shorter time. Additionally, tests on specific real-world targets have also demonstrated that our model can obtain molecules with excellent affinity, drug-likeness, and synthesizability under various conditions simulating real-world virtual screening with a higher proportion. For specific optimization goals in the specific targets, we preformed reinforcement learning, and the results also proved that Token-Mol can achieve optimization under constraint conditions, demonstrating the broad application potential of our model.

We subsequently evaluated its capability in molecular conformation generation. Token-Mol demonstrated superior performance relative to other SOTA models, exceeding their performance by approximately 24% in COV-P and 21% in MAT-P. Notably, Token-Mol exhibited improved efficacy in molecules with a higher number of rotatable bonds.

Lastly, we assessed its performance in molecular property prediction tasks. Leveraging the advantages of the Gaussian cross-entropy loss function, Token-Mol demonstrated accuracy on par with state-of-the-art models. In regression tasks, Token-Mol outperformed the token-only model RT by approximately 30% and surpassed existing sequence-based methods, approaching the performance of GNN-based methods.

Meanwhile, Token-Mol demonstrates a remarkable ability to simplify complex

problems, capitalizing on the inherent advantages of large language models. This proficiency is particularly pronounced in sophisticated tasks such as pocket generation, where Token-Mol achieves an optimal balance of speed and efficacy. Notably, in comparison to the state-of-the-art model TargetDiff, Token-Mol's inference speed is 35 times faster.

While Token-Mol demonstrates significant potential, several areas require further enhancement. In this study, we evaluated its performance on only three representative downstream tasks, leaving many others unaddressed. The molecular diversity within the pre-training data is also limited. Future research will focus on optimizing Token-Mol by expanding the training dataset and developing specific components tailored to particular downstream tasks. Comprehensive evaluations across a broader range of drug design tasks will be conducted. Additionally, we aim to integrate Token-Mol with general artificial intelligence models, utilizing techniques from various large language models such as prompt learning, MoE, and RAG. This integration will facilitate direct interaction between researchers and Token-Mol through conversational interfaces, enhancing its role as a research assistant.

In summary, this study presents a token-only foundational model for drug design, introducing the initial version of Token-Mol. Its development offers a novel approach towards unifying AI drug design models, paving the way for comprehensive drug design using a single foundational model.

Methods

Model architecture

Backbone. Token-Mol is structured with 12 layers of Transformer decoders, each equipped with 8 attention heads. Employing autoregressive approach, Token-Mol predicts both the 2D and 3D structures of molecules while explicitly representing them. To ensure data integrity during autoregressive training and inference, masking matrices are employed to conceal unencoded segments, thus preventing information leakage. The multi-head attention mechanism, integral to the Transformer architecture,

empowers Token-Mol to simultaneously attend to diverse subspaces of the input, facilitating the capture of richer information. Within this mechanism, each attention head learns a unique set of weights to compute attention scores for different positions in the input sequence, facilitating the calculation of the input sequence’s representation. By harnessing parallel computation across multiple attention heads, Token-Mol gains the capacity to interpret the input sequence from various perspectives, consequently enhancing its representational capability and generalization performance. The attention mechanism is shown in Equation 1:

$$Attention(Q, K, V) = \text{softmax}\left(\frac{QK^T}{\sqrt{d_k}}\right)V. \quad (1)$$

where Q , K , and V represent the query, key, and value matrices, respectively, and d_k is the dimension of K .

To indicate the beginning or end of the sequence during sampling, it is necessary to define a start token and an end token, denoted as “<|beginoftext|>” and “<|endofmask|>”, respectively. During the training, the “<|beginoftext|>” token is concatenated to the sequence as the input. The objective during the training phase is to minimize the negative log-likelihood, as shown in Equation 2:

$$\mathcal{L} = -\sum_{i=1}^n \log p(x_i|x_{<i}). \quad (2)$$

During the generation phase, peptides strings are generated using an autoregressive approach based on smiles, which are then concatenated together as shown in Equation 3:

$$p(x) = \prod_{i=1}^n p(x_i|x_{<i}). \quad (3)$$

Gaussian cross-entropy (GCE) loss function. Language models commonly employ the cross-entropy loss function as their primary loss function. The cross-entropy loss function is generally utilized to quantify the disparity between the probability distribution produced by the model and the actual labels. Assuming a classification problem, for each sample, the model outputs a probability distribution indicating the

likelihood of the sample belonging to each class. The genuine labels, on the other hand, are one-hot encoded vectors representing the class to which the sample belongs. The cross-entropy loss function is employed to measure the dissimilarity between the probability distribution produced by the model and the genuine labels. In the context of language models, the specific equation for calculating the cross-entropy loss function is as follows:

$$\mathcal{L} = -\frac{1}{m} \sum_{i=1}^m \sum_{j=1}^n y_{ij} \log q(x_{ij}). \quad (4)$$

Here, m represents the batch size, and n denotes the length of each data point. y_{ij} signifies the j -th element of the true label for the i -th data point (taking values of 0 or 1), and $q(x_{ij})$ represents the j -th element of the probability distribution output by the model. A lower cross-entropy loss indicates a closer resemblance between the model’s output probability distribution and the true labels, thereby reflecting better model performance.

However, the conventional employment of the cross-entropy loss function is primarily confined to discrete category prediction tasks, rendering it inadequate for continuous value prediction endeavors such as regression. In our investigation, we encounter a spectrum of tasks encompassing both classification, exemplified by SMILES strings, and regression, including torsion angles and molecular property prediction. In response to this challenge, the regression transformer disassembles each digit of continuous numerical values into distinct tokens and incorporates specialized numerical embeddings. Nonetheless, their methodology does not fundamentally rectify the issue, as it neglects to facilitate the model’s comprehension of the relative magnitude relationships inherent in numerical values. Notably, the model uniformly assigns loss values in the event of inaccurate predictions, irrespective of the predicted token. For instance, if the label denotes a torsion angle of π , erroneous predictions of 3 or 0 result in identical loss values.

To surmount this constraint, we propose the GCE loss function tailored specifically for regression tasks. As shown in **Fig.S5**, for each prediction, we construct a Gaussian distribution centered around the label’s value, thereby adjusting the probabilities of

surrounding tokens from their original values of 0 to correspond with the Gaussian distribution. Consequently, in Equation 5, where $p(x_{ij})$ is initially denoted as either 0 or 1, we modify it to signify a Gaussian distribution centered around the label’s value, thereby effectively mitigating the issue. The GCE loss function is defined as:

$$\mathcal{L} = -\frac{1}{m} \sum_{i=1}^m \sum_{j=1}^n \frac{1}{\sqrt{2\pi\sigma^2}} e^{-\frac{(x_{ij}-y_{ij})^2}{2\sigma^2}} \log q(x_{ij}). \quad (5)$$

Through the implementation of this configuration, tokens in proximity to the label are allocated greater weights, whereas tokens distanced from the label receive diminished weights. This methodology facilitates the comprehensive learning of relationships between numerical values by the model.

Pocket encoder and fusion block. We utilized the protein pocket encoder trained by Odin et.al⁵⁰, maintaining its parameters frozen throughout the training process. To merge the information derived from the pocket encoder with the existing molecule information within the model, we employed a multi-head condition-attention mechanism. Diverging from traditional cross-attention mechanisms, our approach involved the adoption of a multi-head condition-attention mechanism to fully integrate the information generated at each autoregressive step into subsequent generations. This mechanism treats each token produced during autoregression as a prerequisite condition for iterative generation. Consequently, the entire query, key, and value matrices stem from the original sentence itself. Particularly, as shown in **Fig.1c**, this condition-attention fundamentally regards protein information as prompt data, enabling the model to analyze the interaction between protein information and previously generated tokens.

Reinforcement learning. REINFORCE⁷³, an RL algorithm based on policy gradients, utilizes Monte Carlo methods to determine the optimal policy, and it has been applied in various molecular generation methods^{74 75-77}. In this work, we used the REINFORCE algorithm to optimize the model. We aim to optimize the pre-trained model parameter θ for the task of generating peptide sequences, so that the optimized model can generate molecules with desired properties, as shown in Equation 6:

$$\theta' = \operatorname{argmax}_{\theta} \left(E_{\pi_{\theta}}(G(\tau)) \right). \quad (6)$$

The presented formula elucidates the policy π_{θ} as contingent upon model parameters θ , with τ delineating a trajectory spanning states s_t and actions a_t from the initial time step $t = 0$ to the terminal step $t = T - 1$. Concomitantly, the reward at each juncture t within the trajectory is designated as $r(s_t, a_t)$. Equation 7 concisely portrays the aggregate reward accumulation from time step t to the final state, encapsulating the core essence of the trajectory’s reward accumulation dynamics.

$$G(s_t, a_t) = \sum_{k=t+1}^{T-1} r(s_k, a_k). \quad (7)$$

According to the REINFORCE, the objective function can be derived as follows:

$$J(\theta) = E_{\pi_{\theta}}(G(s_t, a_t)) = \left(\sum_{t=0}^{T-1} \log \pi_{\theta}(a_t | s_t) G(s_t, a_t) \right). \quad (8)$$

Within the molecular generation realm, computing $G(s_t, a_t)$ for each step in a trajectory, corresponding to incomplete molecules, proves impracticable given the inability to reliably estimate the total molecule score from its constituent fragments alone. This scenario converges with the sparse reward paradigm prevalent in reinforcement learning. To surmount this challenge and enable the deployment of the REINFORCE algorithm in this context, we advocate for equating the complete molecule score with the score at each step, thereby reformulating $J(\theta)$ as:

$$J(\theta) = G(\tau) \left(\sum_{t=0}^{T-1} \log \pi_{\theta}(a_t | s_t) \right). \quad (9)$$

Finally, the refinement of $J(\theta)$ is accomplished via gradient descent optimization.

Reward function. To optimize affinity, the reward function is designed to prioritize molecules that meet a promising Vina score. Molecules that exceed the affinity threshold and comply with the QED constraints receive additional rewards. Molecules that do not meet the affinity threshold or are non-compliant are penalized. Thus, the reward function $R(m)$ is described as Equation 10:

$$\mathcal{R}(m) = \begin{cases} \omega \cdot (Vina(m) - init + 0.1 + \theta_{qed}), & \text{if } Vina(m) \leq init \\ 0.1, & \text{if } Vina(m) > init \\ 0, & \text{if } invalid \end{cases} \quad (10)$$

where m is molecule; $Vina(m)$ represents Vina score, where a smaller value is preferable; $init$ is the threshold value of Vina score, which is set as -8. To avoid the issue of sparse rewards, we have imposed a reward weight ω , set as 5, and a proper penalty term set as 0.1 for molecules which do not meet the threshold of Vina score. θ_{qed} is a reward term for molecules that comply with the restraint of QED, describe as Equation 11:

$$\theta_{qed} = \begin{cases} 1, & QED \geq 0.5 \\ 0, & QED < 0.5 \end{cases} \quad (11)$$

Random causal masking

The conventional left-to-right causal masking method exclusively relies on the context preceding the generated tokens, thereby proving inadequate for accomplishing the infilling task. To enhance the adaptability to a wider array of downstream tasks, we opted to train it using random causal masking^{78, 79} in lieu of the left-to-right causal masking.

Throughout the training process, we commence by sampling the number of mask spans from a Poisson distribution centered around a mean of 1, while enforcing a limit that confines the count of mask spans within the range of 1 to 6. Following this, we employ random sampling to establish the length of each span. The locations of the masks are identified using placeholders denoted as “<|mask:k|>”, with “k” signifying the index of the specific mask span. Subsequently, the content subjected to masking is affixed to the sequence’s end, preceded by the “<|mask:k|>” prefix. In the inference phase, a sequence incorporating placeholders “<|mask:k|>” is presented as the contextual input, complemented by the addition of “<|mask:k|>” at the sequence’s conclusion to steer the model’s generation of content for the “<|mask:k|>” segments.

Benchmark

Molecular conformer generation. COV and MAT scores are fundamental metrics

utilized as benchmarks in the Conformer generation task, extensively employed across conformer generation endeavors. COV and MAT metrics are further categorized into Recall and Precision measures. Recall is defined as:

$$\text{COV} - \text{R}(S_g, S_r) = \frac{1}{|S_r|} |\{C \in S_r | \text{RMSD}(C, \hat{C}) \leq \delta, \hat{C} \in S_g\}|. \quad (12)$$

$$\text{MAT} - \text{R}(S_g, S_r) = \frac{1}{|S_r|} \sum_{C \in S_r} \min_{\hat{C} \in S_g} \text{RMSD}(C, \hat{C}). \quad (13)$$

where S_g denotes the ensemble of generated conformations, while S_r represents the ensemble of true conformations. C and \hat{C} represent individual conformations from the sets of true and generated conformations, respectively, with δ acting as the threshold, set at 1.25 Å. The COV metric evaluates the percentage of structures in one set that are encompassed by another set, where inclusion indicates that the RMSD between two conformations falls below a specified threshold δ . Conversely, the MAT scores gauge the average RMSD between conformers in one set and their nearest counterparts in another set. Precision, as described in the provided equation, interchanges S_g and S_r . Consequently, while Recall entails comparing each true conformation with all generated conformations, Precision involves comparing each generated conformation with all true conformations. Precision typically accentuates quality, while Recall is more concerned with diversity.

Pocket-based molecular generation. Valid: validity of generated 3D structure, calculates as the proportion of 3D structures that can be translated into canonical SMILES.

IntDiv: internal diversity³⁵, an assessment of the distinctiveness of molecules within a molecular set, calculated using Tanimoto distance based on ECFP4 fingerprints^{36,37}.

Smi: similarity between two molecular sets, calculate same as IntDiv.

Vina score: the binding energy of ligands to protein pockets by using QVina2³⁸.

High score: the average ratio of generated molecules exceeding the original molecule within each pocket.

MW: Molecular weights.

LogP: the octanol-water partition coefficient, typically falls within the range of -0.4 to 5.6 for the majority of druglike compounds⁸⁰.

Lipinski: Lipinski's rule-of-five⁴¹, which consists of the following criteria: the molecular weight of the compound is less than 500 daltons; the number of hydrogen bond acceptors in the compound's structure (including hydroxyl and amino groups) does not exceed 5; the number of hydrogen bond donors in the compound does not exceed 10; the logarithm of the compound's logP falls within the range of -2 to 5. the number of rotatable bonds in the compound does not exceed 10.

QED: quantitative estimation of drug-likeness³⁹, subsequent researchers have normalized the properties of Lipinski's rule-of-five into continuous values ranging from 0 to 1, where higher values indicate higher drug-likeness of molecules.

SA score: synthetic accessibility score⁴⁰, the SA score represents the synthesis accessibility of molecules and is designated on a scale of 1 to 10, based on chemical expertise. A higher value indicates greater difficulty in synthesis.

Molecular property prediction. During the evaluation, we employ greedy decoding for property prediction. Each method is run independently three times, and the average and standard deviation are reported. We utilize the area under the receiver operating characteristic curve (ROC-AUC)⁸¹ metric to evaluate the classification datasets. For the regression datasets, root mean square error (RMSE) is used to quantify the average difference between predicted values and actual values, which is often applied in regression analysis.

Dataset

Pretraining. The pretraining dataset is sourced from the geometric ensemble of molecules (GEOM) dataset, which includes conformers for 317,000 species, augmented with experimental data spanning biophysics, physiology, and physical chemistry domains⁸². These conformers are generated using sophisticated sampling methods coupled with semi-empirical density functional theory (DFT). Following this,

data curation procedures are implemented to exclude molecules containing heavy metals, lacking torsions, or test molecules. Subsequently, each molecule underwent pre-training with a maximum of 30 conformers, yielding a final dataset containing 8,452,080 entries.

Pocket-based molecular generation. The dataset utilized for pocket-based generation is the same as existing work, which is an open-available dataset consisted of over 20 million of pose pairs from nearly 20,000 protein-ligand complexes from CrossDock2020⁸³. Following the protocol outlined in previous studies^{33, 50}, we discarded all poses with an RMSD greater than 2Å, and additionally partitioned the dataset into training and testing sets based on a principle of sequence similarity less than 40%, ensuring a fairer evaluation of the generalizability to unknown pockets. Additionally, we excluded protein-ligand pairs which ligand lacked torsion angles from the dataset, resulted in slightly smaller training and testing sets compared to several models we mention subsequently.

The real-world targets' structure are download from RCSB PDB⁸⁴, and reference molecules corresponding to each targets are collected from ChEMBL30 database⁸⁵. Molecules with a K_d or K_i value less than 1,000 nM for a given target are considered active, counting into the reference sets. If the number of molecules meeting this criterion is low, molecules with an IC50 value less than 1,000 nM are also included in the reference sets. The collected molecules are deduplicated based on SMILES and molecules containing salts are removed.

Molecular conformation generation. We performed fine-tuning using datasets consistent with those utilized in earlier studies^{30, 62, 64, 66}. For the test set, we employed a dataset akin to Tora3D²⁶. Test set I contains 200 molecules, each with fewer than 100 conformations. Test set II comprises 1,000 randomly selected molecules with conformation counts distributed similarly to the entire dataset, spanning from 0 to 500.

Molecular Property prediction. We assembled a comprehensive collection of 12 datasets sourced from MolecularNet⁸⁶ and therapeutics data commons (TDC)⁸⁷, accompanied by comprehensive datasets descriptions provided in the **Supplementary**. Drawing upon MolecularNet's established status as a primary benchmark for molecular

property prediction, our selection comprised six classification datasets and three regression datasets. Furthermore, within TDC, widely acclaimed as the premier public benchmark for ADMET analysis, we specifically identified three datasets characterized by relatively homogeneous data distributions. Each dataset underwent three random partitions following the 8:1:1 ratio for testing.

Data availability

The datasets utilized in our study are as follows: The GEOM dataset is available at <https://dataverse.harvard.edu/dataset.xhtml?persistentId=doi:10.7910/DVN/JNGTDF>. For pocket-based molecular generation dataset is provided at https://drive.google.com/drive/folders/1CzwxmTpjbrt83z_wBzcQncq84OVDPurM. The molecular conformation generation, the dataset can be accessed at <https://github.com/zimeizhng/Tora3D>. Lastly, the datasets for property prediction are available at <https://moleculenet.org/datasets-1> and https://tdcommons.ai/single_pred_tasks/adme/.

Code availability

The code will be released at a later date.

Acknowledgements

This work was financially supported by National Key Research and Development Program of China (2022YFF1203003), National Natural Science Foundation of China (22220102001, 82204279, 81973281, 82373791, 22303083), (226-2022-00220), China Postdoctoral Science Foundation (2023M733128, 2023TQ0285), Postdoctoral Fellowship Program of CPSF (GZB20230657).

Author Contributions

T.J.H., C.Y.H. and Y.K. designed the research study. J.K.W. developed the method and

wrote the code. J.K.W., R.Q., M.Y.W., M.J.F., Y.Y.Z., G.Q.L., Q. S. performed the analysis. J.K.W., R.Q., M.Y.W., M.J.F., Y.Y.Z., Y.K., C.Y.H. and T.J.H. wrote the paper. All authors read and approved the manuscript.

Competing interests

The authors declare that they have no competing interests.

References

1. Devlin, J., Chang, M.-W., Lee, K. & Toutanova, K. Bert: Pre-training of deep bidirectional transformers for language understanding. Preprint at <https://arxiv.org/abs/1810.04805> (2018).
2. Radford, A., Narasimhan, K., Salimans, T. & Sutskever, I. Improving language understanding by generative pre-training. Preprint at https://s3-us-west-2.amazonaws.com/openai-assets/research-covers/language-unsupervised/language_understanding_paper.pdf (2018).
3. Chithrananda, S., Grand, G. & Ramsundar, B. Chemberta: Large-scale self-supervised pretraining for molecular property prediction. Preprint at <https://arxiv.org/abs/2010.09885> (2020).
4. Rong, Y. et al. Self-supervised graph transformer on large-scale molecular data. Proceedings of the 34th International Conference on Neural Information Processing Systems (Curran Associates Inc., 2020).
5. Rives, A. et al. Biological structure and function emerge from scaling unsupervised learning to 250 million protein sequences. *Proc. Natl. Acad. Sci. U.S.A.* **118**, e2016239118 (2021).
6. Kim, H., Lee, J., Ahn, S. & Lee, J.R. A merged molecular representation learning for molecular properties prediction with a web-based service. *Sci. Rep.* **11**, 11028 (2021).
7. Liu, S. et al. Pre-training molecular graph representation with 3d geometry. Preprint at <https://arxiv.org/abs/2110.07728> (2021).
8. Ferruz, N., Schmidt, S. & Höcker, B. Protgpt2 is a deep unsupervised language model for protein design. *Nat. Commun.* **13**, 4348 (2022).
9. Wang, Y., Wang, J., Cao, Z. & Barati Farimani, A. Molecular contrastive learning of representations via graph neural networks. *Nat. Mach. Intell.* **4**, 279-287 (2022).
10. Ross, J. et al. Large-scale chemical language representations capture molecular structure and properties. *Nat. Mach. Intell.* **4**, 1256-1264 (2022).
11. Zeng, X. et al. Accurate prediction of molecular properties and drug targets using a self-supervised image representation learning framework. *Nat. Mach. Intell.* **4**, 1004-1016 (2022).
12. Li, H. et al. A knowledge-guided pre-training framework for improving molecular representation learning. *Nat. Commun.* **14**, 7568 (2023).
13. Lin, X. et al. Pangu drug model: Learn a molecule like a human. *Sci. China Life Sci.* **66**, 879-882 (2023).
14. Shuai, R.W., Ruffolo, J.A. & Gray, J.J. Iglm: Infilling language modeling for antibody sequence design. *Cell Syst.* **14**, 979-989.e974 (2023).

15. Nijkamp, E., Ruffolo, J.A., Weinstein, E.N., Naik, N. & Madani, A. Progen2: Exploring the boundaries of protein language models. *Cell Syst.* **14**, 968-978.e963 (2023).
16. Ying, C. et al. Do transformers really perform bad for graph representation? Proceedings of the 35th International Conference on Neural Information Processing Systems (Curran Associates Inc., 2024).
17. Xia, J., Zhu, Y., Du, Y. & Li, S.Z. A systematic survey of chemical pre-trained models. Preprint at <https://arxiv.org/abs/2210.16484> (2022).
18. Weininger, D. Smiles, a chemical language and information system. 1. Introduction to methodology and encoding rules. *J. Chem. Inf. Comput. Sci.* **28**, 31-36 (1988).
19. Krenn, M., Häse, F., Nigam, A., Friederich, P. & Aspuru-Guzik, A. Self-referencing embedded strings (selfies): A 100% robust molecular string representation. *Mach. Learn.: Sci. Technol.* **1**, 045024 (2020).
20. Wang, S., Guo, Y., Wang, Y., Sun, H. & Huang, J. Smiles-bert: Large scale unsupervised pre-training for molecular property prediction. Proceedings of the 10th ACM International Conference on Bioinformatics, Computational Biology and Health Informatics (ACM, 2019).
21. Bagal, V., Aggarwal, R., Vinod, P.K. & Priyakumar, U.D. Molgpt: Molecular generation using a transformer-decoder model. *J. Chem. Inf. Model.* **62**, 2064-2076 (2022).
22. Irwin, R., Dimitriadis, S., He, J. & Bjerrum, E.J. Chemformer: A pre-trained transformer for computational chemistry. *Mach. Learn.: Sci. Technol.* **3**, 015022 (2022).
23. Hu, W. et al. Strategies for pre-training graph neural networks. Preprint at <https://arxiv.org/abs/1905.12265> (2019).
24. Rong, Y. et al. Self-supervised graph transformer on large-scale molecular data. Preprint at <https://arxiv.org/abs/2007.02835> (2020).
25. Xia, J. et al. Mole-bert: Rethinking pre-training graph neural networks for molecules. Preprint at <https://openreview.net/pdf?id=jevY-DtiZTR> (2023).
26. Fang, X. et al. Geometry-enhanced molecular representation learning for property prediction. *Nat. Mach. Intell.* **4**, 127-134 (2022).
27. Zhou, G. et al. Uni-mol: A universal 3d molecular representation learning framework. International Conference on Learning Representations (ICLR, 2023).
28. Research AI4Science, M. & Azure Quantum, M. The impact of large language models on scientific discovery: A preliminary study using gpt-4. Preprint at <https://arxiv.org/abs/2311.07361> (2023).
29. Born, J. & Manica, M. Regression transformer enables concurrent sequence regression and generation for molecular language modelling. *Nat. Mach. Intell.* **5**, 432-444 (2023).
30. Flam-Shepherd, D. & Aspuru-Guzik, A. Language models can generate molecules, materials, and protein binding sites directly in three dimensions as xyz, cif, and pdb files. Preprint at <https://arxiv.org/abs/2305.05708> (2023).
31. Ganea, O.-E. et al. Geomol: Torsional geometric generation of molecular 3d conformer ensembles. Preprint at <https://arxiv.org/abs/2106.07802> (2021).
32. Liu, M., Luo, Y., Uchino, K., Maruhashi, K. & Ji, S. Generating 3d molecules for target protein binding. Preprint at <https://arxiv.org/abs/2204.09410> (2022).
33. Peng, X. et al. Pocket2mol: Efficient molecular sampling based on 3d protein pockets. International Conference on Machine Learning (PMLR, 2022).
34. Guan, J. et al. 3d equivariant diffusion for target-aware molecule generation and affinity

- prediction. Preprint at <https://arxiv.org/abs/2303.03543> (2023).
35. Polykovskiy, D. et al. Molecular sets (moses): A benchmarking platform for molecular generation models. *Front. Pharmacol.* **11** (2020).
 36. Rogers, D. & Hahn, M. Extended-connectivity fingerprints. *J. Chem. Inf. Model.* **50**, 742-754 (2010).
 37. Bajusz, D., Rácz, A. & Héberger, K. Why is tanimoto index an appropriate choice for fingerprint-based similarity calculations? *J. Cheminf.* **7**, 20 (2015).
 38. Alhossary, A., Handoko, S.D., Mu, Y. & Kwoh, C.-K. Fast, accurate, and reliable molecular docking with quickvina 2. *Bioinformatics* **31**, 2214-2216 (2015).
 39. Bickerton, G.R., Paolini, G.V., Besnard, J., Muresan, S. & Hopkins, A.L. Quantifying the chemical beauty of drugs. *Nat. Chem.* **4**, 90-98 (2012).
 40. Ertl, P. & Schuffenhauer, A. Estimation of synthetic accessibility score of drug-like molecules based on molecular complexity and fragment contributions. *J. Cheminf.* **1**, 8 (2009).
 41. Lipinski, C.A., Lombardo, F., Dominy, B.W. & Feeney, P.J. Experimental and computational approaches to estimate solubility and permeability in drug discovery and development settings. *Adv. Drug Delivery Rev.* **23**, 3-25 (1997).
 42. Shultz, M.D. Two decades under the influence of the rule of five and the changing properties of approved oral drugs. *J. Med. Chem.* **62**, 1701-1714 (2019).
 43. Ertl, P., Rohde, B. & Selzer, P. Fast calculation of molecular polar surface area as a sum of fragment-based contributions and its application to the prediction of drug transport properties. *J. Med. Chem.* **43**, 3714-3717 (2000).
 44. Veber, D.F. et al. Molecular properties that influence the oral bioavailability of drug candidates. *J. Med. Chem.* **45**, 2615-2623 (2002).
 45. Hitchcock, S.A. & Pennington, L.D. Structure–brain exposure relationships. *J. Med. Chem.* **49**, 7559-7583 (2006).
 46. Liu, S. et al. Discovery of novel benzo[4,5]imidazo[1,2-a]pyrazin-1-amine-3-amide-one derivatives as anticancer human a2a adenosine receptor antagonists. *J. Med. Chem.* **65**, 8933-8947 (2022).
 47. Clyde, A. et al. High-throughput virtual screening and validation of a sars-cov-2 main protease noncovalent inhibitor. *J. Chem. Inf. Model.* **62**, 116-128 (2022).
 48. Sun, C. et al. Novel small-molecule pd-11 inhibitor induces pd-11 internalization and optimizes the immune microenvironment. *J. Med. Chem.* **66**, 2064-2083 (2023).
 49. Zhang, O. et al. Learning on topological surface and geometric structure for 3d molecular generation. *Nat. Comput. Sci.* **3**, 849-859 (2023).
 50. Zhang, O. et al. Resgen is a pocket-aware 3d molecular generation model based on parallel multiscale modelling. *Nat. Mach. Intell.* **5**, 1020-1030 (2023).
 51. Zhavoronkov, A. et al. Deep learning enables rapid identification of potent ddr1 kinase inhibitors. *Nat. Biotechnol.* **37**, 1038-1040 (2019).
 52. Li, S. et al. Ls-molgen: Ligand-and-structure dual-driven deep reinforcement learning for target-specific molecular generation improves binding affinity and novelty. *J. Chem. Inf. Model.* **63**, 4207-4215 (2023).
 53. Baraldi, S. et al. in *The adenosine receptors*. (eds. P.A. Borea, K. Varani, S. Gessi, S. Merighi & F. Vincenzi) 91-136 (Springer International Publishing, Cham; 2018).
 54. Yu, F., Zhu, C., Xie, Q. & Wang, Y. Adenosine a2a receptor antagonists for cancer

- immunotherapy. *J. Med. Chem.* **63**, 12196-12212 (2020).
55. Spinaci, A. et al. in Purinergic receptors and their modulators. (eds. V. Colotta & C.T. Supuran) 101-141 (Springer International Publishing, Cham; 2023).
56. Bemis, G.W. & Murcko, M.A. The properties of known drugs. 1. Molecular frameworks. *J. Med. Chem.* **39**, 2887-2893 (1996).
57. Preuer, K., Renz, P., Unterthiner, T., Hochreiter, S. & Klambauer, G. Fréchet chemnet distance: A metric for generative models for molecules in drug discovery. *J. Chem. Inf. Model.* **58**, 1736-1741 (2018).
58. Friesner, R.A. et al. Glide: A new approach for rapid, accurate docking and scoring. 1. Method and assessment of docking accuracy. *J. Med. Chem.* **47**, 1739-1749 (2004).
59. Spitzer, R. & Jain, A.N. Surflex-dock: Docking benchmarks and real-world application. *J. Comput.-Aided Mol. Des.* **26**, 687-699 (2012).
60. Mansimov, E., Mahmood, O., Kang, S. & Cho, K. Molecular geometry prediction using a deep generative graph neural network. *Sci. Rep.* **9**, 20381 (2019).
61. Simm, G.N.C. & Hernández-Lobato, J.M. A generative model for molecular distance geometry. Preprint at <https://arxiv.org/abs/1909.11459> (2019).
62. Xu, M., Luo, S., Bengio, Y., Peng, J. & Tang, J. Learning neural generative dynamics for molecular conformation generation. Preprint at <https://arxiv.org/abs/2102.10240> (2021).
63. Xu, M. et al. An end-to-end framework for molecular conformation generation via bilevel programming. Preprint at <https://arxiv.org/abs/2105.07246> (2021).
64. Xu, M. et al. Geodiff: A geometric diffusion model for molecular conformation generation. Preprint at <https://arxiv.org/abs/2203.02923> (2022).
65. Jing, B., Corso, G., Chang, J., Barzilay, R. & Jaakkola, T. Torsional diffusion for molecular conformer generation. Preprint at <https://arxiv.org/abs/2206.01729> (2022).
66. Zhang, Z. et al. Tora3d: An autoregressive torsion angle prediction model for molecular 3d conformation generation. *J. Cheminf.* **15**, 57 (2023).
67. Chen, T. & Guestrin, C. Xgboost: A scalable tree boosting system. Proceedings of the 22nd ACM SIGKDD International Conference on Knowledge Discovery and Data Mining (ACM, 2016).
68. Wu, Z. et al. Knowledge-based bert: A method to extract molecular features like computational chemists. *Brief. Bioinform.* **23** (2022).
69. Heid, E. et al. Chemprop: A machine learning package for chemical property prediction. *J. Chem. Inf. Model.* **64**, 9-17 (2024).
70. Notwell, J.H. & Wood, M.W. Admet property prediction through combinations of molecular fingerprints. Preprint at <https://arxiv.org/abs/2310.00174> (2023).
71. Jacobs, R.A., Jordan, M.I., Nowlan, S.J. & Hinton, G.E. Adaptive mixtures of local experts. *Neural Comput.* **3**, 79-87 (1991).
72. Lewis, P. et al. Retrieval-augmented generation for knowledge-intensive nlp tasks. Proceedings of the 34th International Conference on Neural Information Processing Systems (PMLR, 2020).
73. Williams, R.J. Simple statistical gradient-following algorithms for connectionist reinforcement learning. *Machine Learning* **8**, 229-256 (1992).
74. Olivecrona, M., Blaschke, T., Engkvist, O. & Chen, H. Molecular de-novo design through deep reinforcement learning. *J. Cheminf.* **9**, 48 (2017).
75. Popova, M., Isayev, O. & Tropsha, A. Deep reinforcement learning for de novo drug design. *Sci.*

- Adv.* **4**, eaap7885 (2018).
76. Wang, J. et al. Multi-constraint molecular generation based on conditional transformer, knowledge distillation and reinforcement learning. *Nat. Mach. Intell.* **3**, 914-922 (2021).
 77. Wang, J. et al. Molecular generation with reduced labeling through constraint architecture. *J. Chem. Inf. Model.* **63**, 3319-3327 (2023).
 78. Aghajanyan, A. et al. Cm3: A causal masked multimodal model of the internet. Preprint at <https://arxiv.org/abs/2201.07520> (2022).
 79. Fried, D. et al. Incoder: A generative model for code infilling and synthesis. Preprint at <https://arxiv.org/abs/2204.05999> (2022).
 80. Ghose, A.K., Viswanadhan, V.N. & Wendoloski, J.J. A knowledge-based approach in designing combinatorial or medicinal chemistry libraries for drug discovery. 1. A qualitative and quantitative characterization of known drug databases. *J. Comb. Chem.* **1**, 55-68 (1999).
 81. Bradley, A.P. The use of the area under the roc curve in the evaluation of machine learning algorithms. *Pattern Recognit.* **30**, 1145-1159 (1997).
 82. Axelrod, S. & Gómez-Bombarelli, R. Geom, energy-annotated molecular conformations for property prediction and molecular generation. *Sci. Data* **9**, 185 (2022).
 83. Francoeur, P.G. et al. Three-dimensional convolutional neural networks and a cross-docked data set for structure-based drug design. *J. Chem. Inf. Model.* **60**, 4200-4215 (2020).
 84. Burley, S.K. et al. Rcsb protein data bank (rcsb.Org): Delivery of experimentally-determined pdb structures alongside one million computed structure models of proteins from artificial intelligence/machine learning. *Nucleic Acids Res.* **51**, D488-D508 (2022).
 85. Zdrzil, B. et al. The chembl database in 2023: A drug discovery platform spanning multiple bioactivity data types and time periods. *Nucleic Acids Res.* **52**, D1180-D1192 (2023).
 86. Wu, Z. et al. Moleculenet: A benchmark for molecular machine learning. *Chem. Sci.* **9**, 513-530 (2018).
 87. Huang, K. et al. Therapeutics data commons: Machine learning datasets and tasks for drug discovery and development. Preprint at <https://arxiv.org/abs/2102.09548> (2021).

Supplementary

1. Attention Analysis of molecular prediction task

In the main manuscript, we validated Token-Mol's robust predictive capabilities in molecular property prediction tasks. While predictive accuracy is essential for scientific research, it is equally crucial for a model to validate scientific hypotheses. To this end, we focused on drug solubility and acute oral toxicity, areas extensively explored and significant for verifying model interpretability¹. Using the ESOL and LD50 datasets, we illustrated how Token-Mol can extract relevant features from specific atoms or functional groups and assign corresponding attention weights to related tokens.

The ESOL dataset relates to molecular solubility, where various functional groups significantly influence solubility. Molecules containing polar functional groups, such as hydroxyl, carboxyl, and amino groups, generally exhibit higher solubility² due to their ability to form hydrogen bonds with water molecules. In contrast, hydrophobic functional groups, such as alkyl and halogen groups, tend to reduce solubility. **Fig. S7a** shows that in hydrophilic substructures, sp² hybridized carbon, hydroxyl groups, and amine groups substantially impact the molecule's attention weights. For low-solubility molecules, the figure indicates that chlorophenyl and halogen atoms receive high attention weights. Moreover, a comparison in **Fig. S7a** reveals that, unlike high-solubility molecules where single functional groups often have significant influence, in drug design, the hydrophobicity of a molecule typically has a more holistic impact, with modifications of key hydrophobic groups affecting the overall structure's hydrophobic properties.

In drug toxicity research, we typically focus on toxicophores, or structural alerts (SAs)³, defined as key substructures responsible for specific toxicities and commonly used to elucidate these relationships. For example, in the LD50 dataset, we identified the nitrosamide and phosphoric trimer toxicophores as reported by Wu et al.⁴. Nitrosamide is a frequently occurring SA in both mutagenic and non-mutagenic compounds⁵, while phosphoric trimer is commonly found in compounds with acute oral toxicity⁶. We filtered the dataset for molecules containing nitrosamide and

phosphoric trimer toxicophores and visualized the model's attention weights for these molecules. As shown in **Fig. S7b**, the model indeed assigns high attention weights to these toxicophores in all molecules containing the identified toxic fragments.

2. Datasets Details

The descriptions of various benchmarks dataset are listed in **Table S6**.

- BACE is a database that catalogues molecules with 2D structures and properties, focusing on inhibitors of human β -secretase 1. It provides qualitative (binary label) binding results for these inhibitors.
- The BBBP dataset comprises molecules with measured permeability properties, specifically assessing their ability to penetrate the blood-brain barrier.
- ClinTox is a dataset that encompasses both FDA-approved drugs and compounds that have been discontinued from clinical trials due to toxicity concerns.
- SIDER is a database that catalogs marketed drugs along with their associated adverse drug reactions (ADRs), categorized into 27 system organ classes.
- Tox21 assesses the toxicity of compounds across 12 different targets, spanning nuclear receptors and stress response pathways. It served as a public database for the 2014 Tox21 Data Challenge.
- ToxCast comprises toxicology data for thousands of molecules, offering multiple toxicity labels derived from high-throughput screening experiments conducted on a vast chemical library.
- The ESOL (Free Solvation Energy of Neutral Organic Molecules in Water) dataset is a standard dataset used in machine learning and cheminformatics research. It aims to predict the free solvation energy of organic molecules in water.
- The Free Solvation Database, FreeSolv (SAMPL), provides experimental and calculated hydration free energy of small molecules in water. The calculated values are derived from alchemical free energy calculations using molecular dynamics simulations.
- Lipophilicity measures the ability of a drug to dissolve in a lipid (e.g. fats, oils) environment. High lipophilicity often leads to high rate of metabolism, poor

solubility, high turn-over, and low absorption.

- The human colon epithelial cancer cell line, Caco-2, is used as an in vitro model to simulate the human intestinal tissue. The experimental result on the rate of drug passing through the Caco-2 cells can approximate the rate at which the drug permeates through the human intestinal tissue.
- Aqueous solubility measures a drug's ability to dissolve in water. Poor water solubility could lead to slow drug absorptions, inadequate bioavailability and even induce toxicity. More than 40% of new chemical entities are not soluble.
- Acute toxicity LD50 measures the most conservative dose that can lead to lethal adverse effects. The higher the dose, the more lethal of a drug.

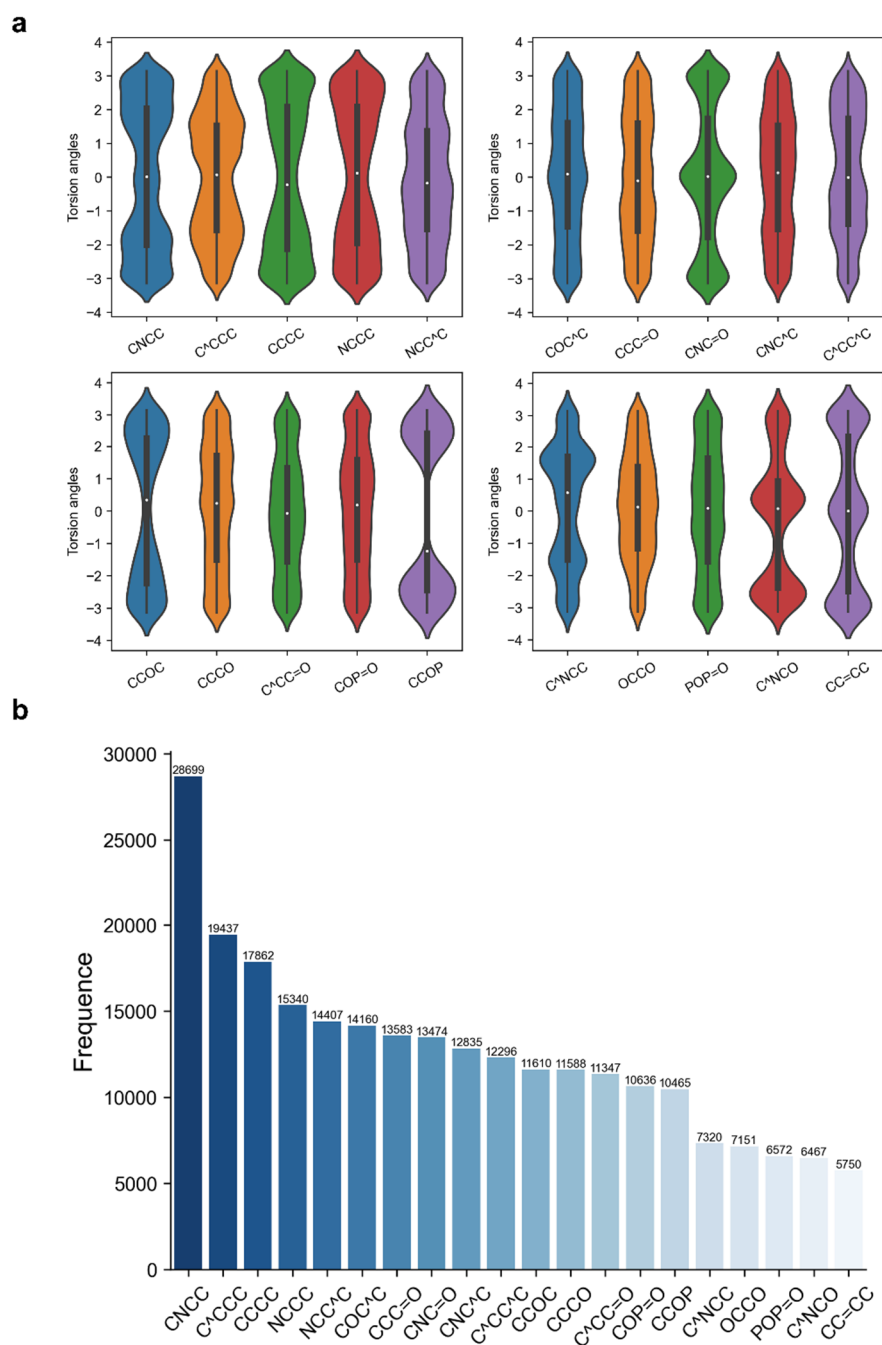


Fig. S1 | The distributions of torsion angles in the training set. (a) Values distributions (From -3.14 to 3.14) and **(b)** frequencies of the common torsion angles in the training set.

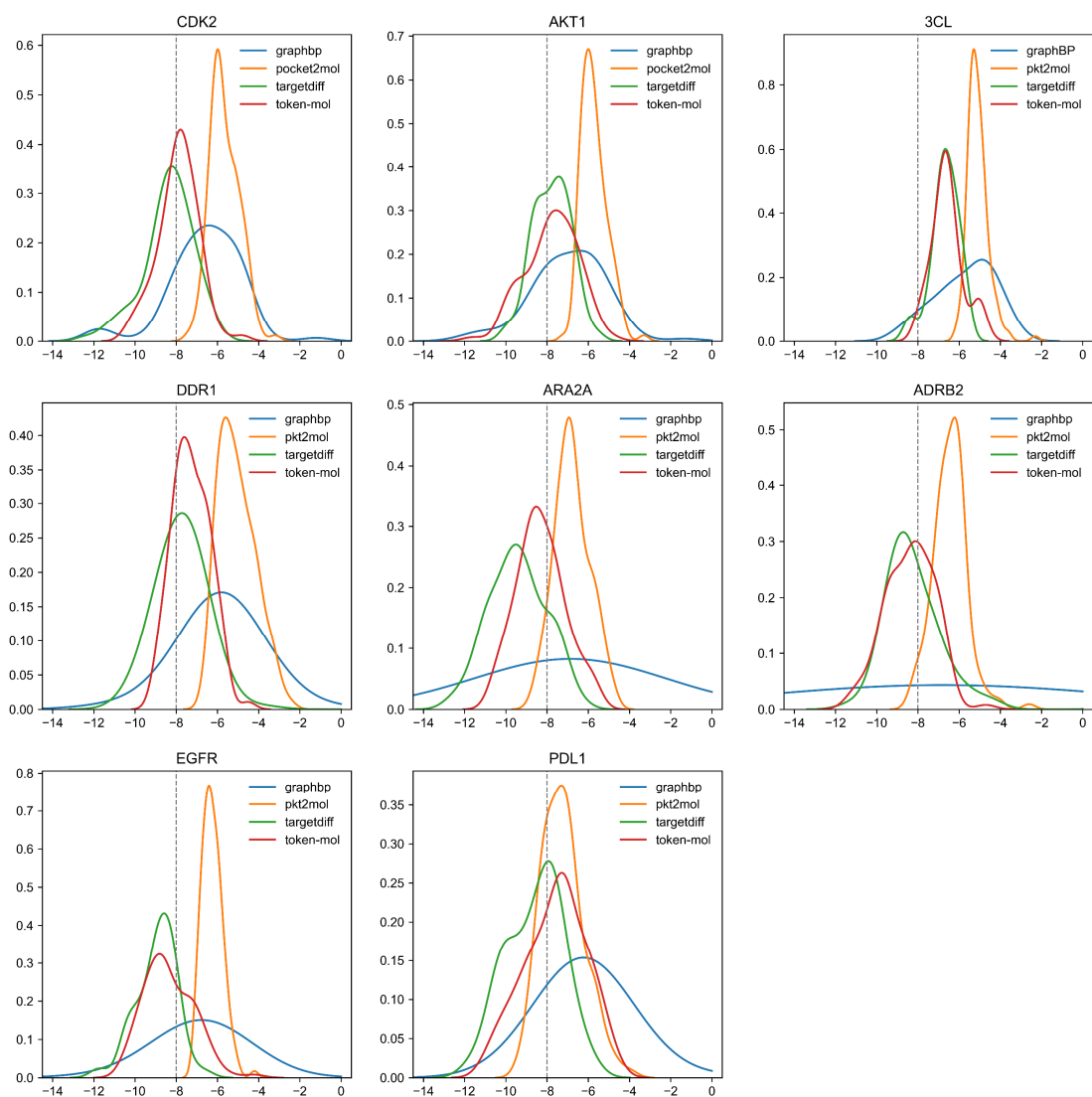


Fig. S2 | Vina score distributions of Token-Mol and baseline models on the selected real-world targets. The gray dashed line and the area to its left represent 'high affinity' molecules, defined as molecules with a Vina score of less than or equal to -8.

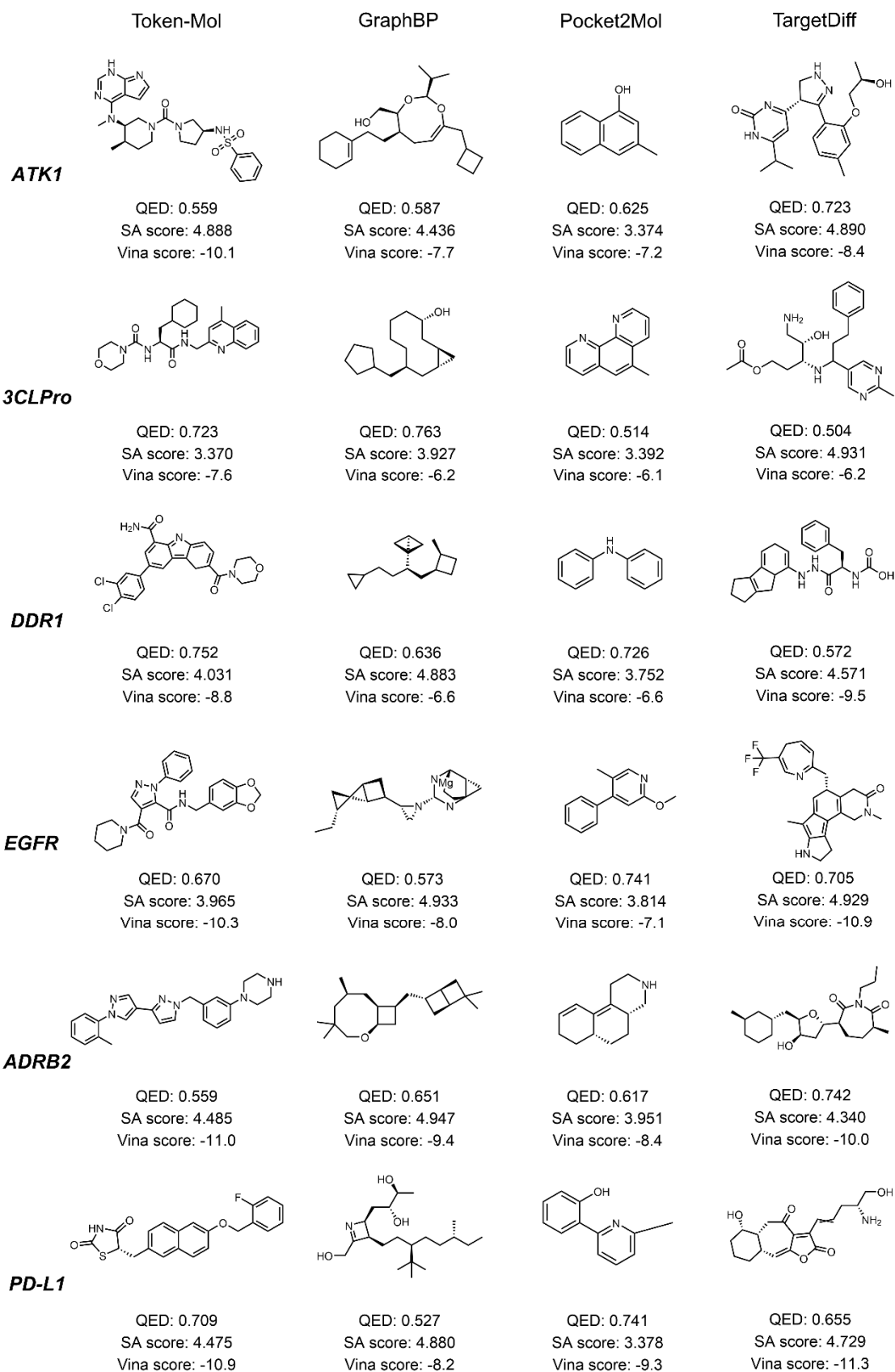


Fig. S3 |The ‘drug-like’ molecules with the highest affinity and their properties on the selected real-world targets which are not represented in the main text.

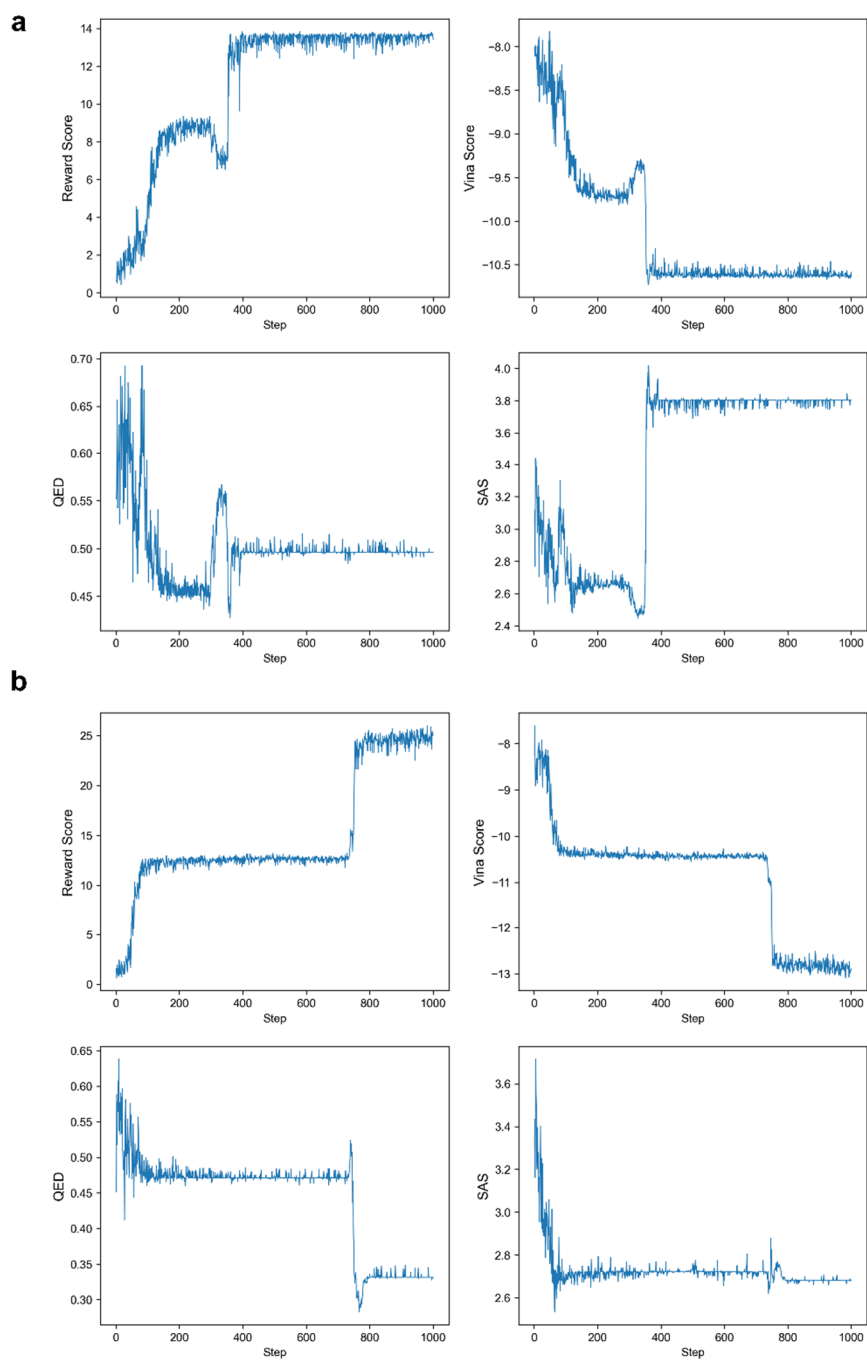


Fig. S4 | Metrics during the reinforcement learning to optimized the binding affinity without any constraints in (a) CDK2 and (b) EGFR.

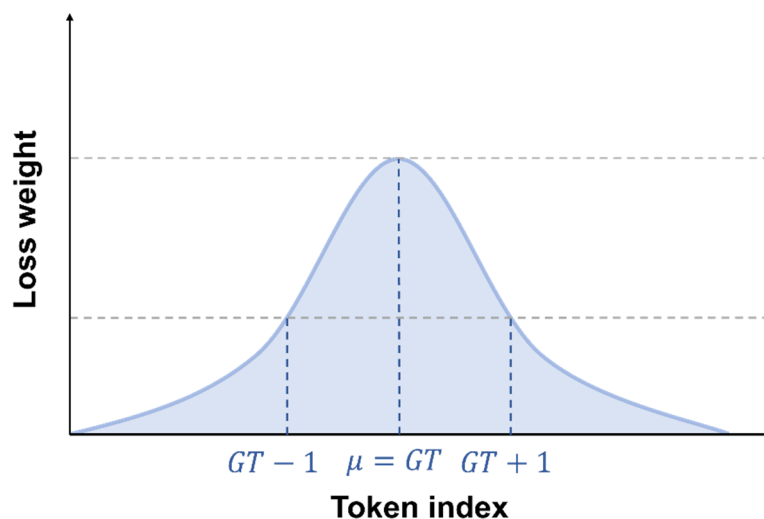


Fig. S5 | Gaussian cross-entropy loss function.

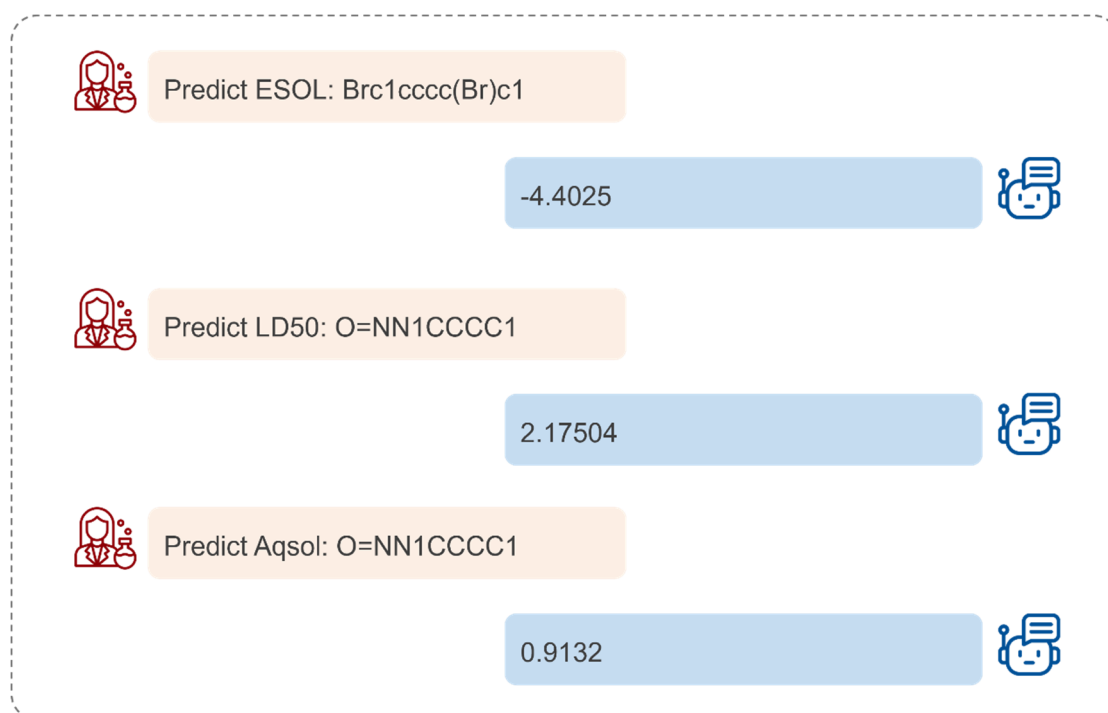


Fig. S6 | The example of “Chat to Token-Mol”.

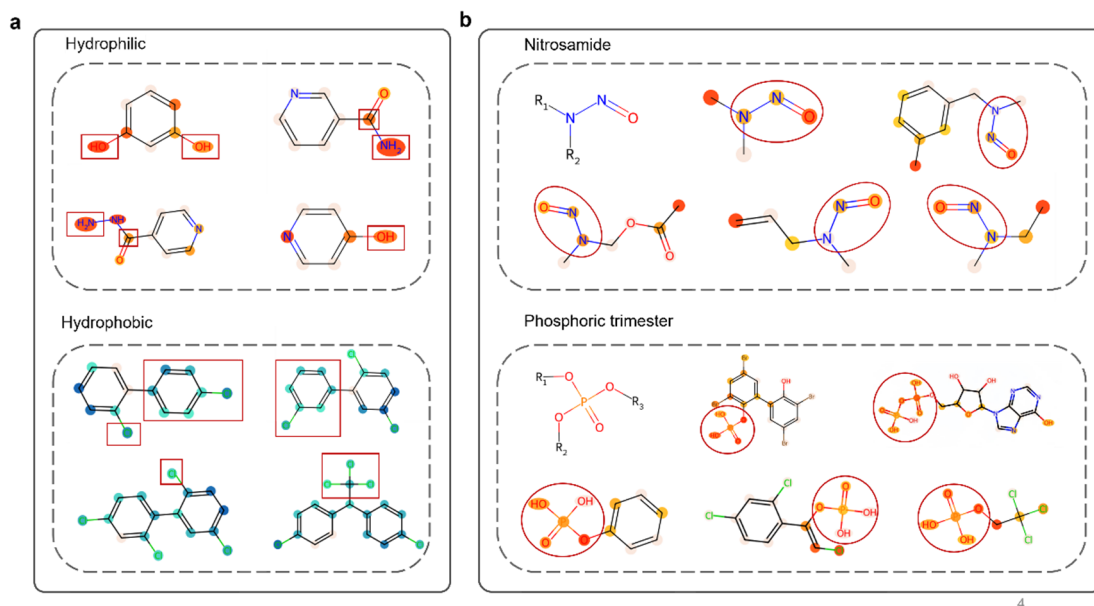


Fig. S7 | Visualization of the attention weights for different molecules. (a) The attribution visualization of aqueous solubility. The darker the color, the higher the weight. **(b)** Nitrosamide and phosphoric trimer of acute oral toxicity.

Table S1 | Detailed data about the molecular properties of molecules generated in the test set by Token-Mol and other baseline models.

Metric		Ori.	Token-Mol	GraphBP	Pocket2Mol	TargetDiff
Vina score ↓	<i>Avg.</i>	7.010	-7.226	-6.659	-7.729	-7.236
	<i>Med.</i>	-6.900	-7.189	-6.733	-7.131	-7.251
QED ↑	<i>Avg.</i>	0.492	0.568	0.511	0.536	0.493
	<i>Med.</i>	0.470	0.568	0.510	0.561	0.493
SA score ↓	<i>Avg.</i>	4.214	4.166	5.271	5.846	4.858
	<i>Med.</i>	4.277	4.232	5.301	5.716	5.029
Lipinski ↑	<i>Avg.</i>	4.247	4.666	4.749	4.782	4.586
	<i>Med.</i>	5.000	4.684	4.746	4.958	4.776
MW	<i>Avg.</i>	337.341	355.414	257.307	274.273	329.241
	<i>Med.</i>	326.013	366.857	257.772	242.405	340.350
TPSA	<i>Avg.</i>	114.292	87.320	39.834	72.246	94.945
	<i>Med.</i>	87.300	87.660	39.811	67.345	88.997

Table S2 | The rate of high affinity molecules and the average QED values of generated molecules from different models on the selected real-world targets.

	High Affinity (%) #				QED			
	Token-Mol	GraphBP	Pocket2Mol	TargetDiff	Token-Mol	GraphBP	Pocket2Mol	TargetDiff
CDK2	33.97	15.29	0	58.60	0.630	0.464	0.578	0.472
AKT1	36.78	22.35	0	39.13	0.592	0.481	0.578	0.472
EGFR	63.96	15.66	0	85.90	0.537	0.433	0.614	0.282
DDR1	18.52	6.82	0	38.46	0.589	0.430	0.585	0.331
ARA2A	61.82	21.18	7.34	80.00	0.560	0.447	0.628	0.618
ADRB2	61.11	19.32	2.13	65.93	0.571	0.478	0.641	0.324
3CL	1.85	7.69	0	6.35	0.554	0.455	0.660	0.247
PD-L1	36.11	4.34	23.01	58.90	0.553	0.457	0.620	0.391

High affinity means Vina score lower than -8 (See also Supplementary Data Fig. S2).

Table S3 | Detailed data for drug-like molecules with the highest affinity generated for the two selected targets from different models.

Target	Model	Vina Score	QED	SA Score	Lipinski	TPSA
CDK2	Token-Mol	-9.4	0.746	4.434	5	92.26
	GraphBP	-8.1	0.836	4.102	5	37.30
	Pocket2Mol	-7.4	0.625	3.374	5	20.23
	TargetDiff	-8.9	0.586	4.868	5	112.74
ARA2A	Token-Mol	-9.5	0.541	4.306	5	49.69
	GraphBP	-8.0	0.527	4.367	5	0
	Pocket2Mol	-7.1	0.741	3.814	5	0
	TargetDiff	-11.2	0.792	4.809	5	58.89

Table S4 | The similarity between the generated molecules and reference molecules.

	Scaffold Similarity↑				FCD↓			
	Token-Mol	GraphBP	Pocket2Mol	TargetDiff	Token-Mol	GraphBP	Pocket2Mol	TargetDiff
CDK2	0.121	0.026	0.099	0.101	42.863	52.530	47.603	46.167
AKT1	0.101	0.039	0.083	0.097	51.058	51.327	48.625	53.346
3CL	0.103	0.050	0.083	0.086	37.741	46.988	44.441	40.010
DDR1	0.127	0.034	0.051	0.111	47.912	56.974	55.331	49.085
ARA2A	0.111	0.033	0.096	0.102	53.982	64.379	61.755	54.312
ADRB2	0.106	0.038	0.071	0.082	43.835	48.020	47.028	43.131
EGFR	0.110	0.037	0.090	0.102	66.625	68.195	62.690	70.251
PD-L1	0.106	0.029	0.072	0.094	47.734	50.706	49.660	48.366

Scaffold similarity is the similarity of the Bemis-Murcko scaffolds between reference molecules and generated molecules, calculated with ECFP4 fingerprints. FCD, Fréchet ChemNet Distance.

Table S5 | Information about the reference molecules.

Target	Number	QED	Mean Vina Score
CDK2	402	0.482	-8.589
AKT1	156	0.461	-7.612
3CL	448	0.438	-6.966
DDR1	261	0.401	-8.010
ARA2A	3679	0.533	-8.695
ADRB2	457	0.405	-8.977
EGFR	421	0.482	-8.247
PD-L1	52	0.408	4.515

Table S6 | Dataset details of molecular property prediction task.

Task Type	Metric	Dataset	Benchmark	Compounds	Tasks
Classification	ROC-AUC	BACE	MolecularNet	1513	1
		BBBP	MolecularNet	2039	1
		ClinTox	MolecularNet	1478	2
		SIDER	MolecularNet	1427	27
		Tox21	MolecularNet	7831	12
		ToxCast	MolecularNet	8575	617
Regression	RMSE	ESOL	MolecularNet	1128	1
		FreeSolv	MolecularNet	642	1
		Lipophilicity	MolecularNet	4200	1
		Caco-2	TDC	906	1
		AqSolDB (Solubility)	TDC	9982	1
		Acute Toxicity LD50	TDC	7385	1

1. Wu, Z. et al. Chemistry-intuitive explanation of graph neural networks for molecular property prediction with substructure masking. *Nat. Commun.* **14**, 2585 (2023).
2. Tayyebi, A. et al. Prediction of organic compound aqueous solubility using machine learning: A comparison study of descriptor-based and fingerprints-based models. *J. Cheminf.* **15**, 99 (2023).
3. Yang, H., Sun, L., Li, W., Liu, G. & Tang, Y. In silico prediction of chemical toxicity for drug design using machine learning methods and structural alerts. *Front. Chem.* **6** (2018).
4. Wu, Z. et al. Mining toxicity information from large amounts of toxicity data. *J. Med. Chem.* **64**, 6924-6936 (2021).
5. Xu, C. et al. In silico prediction of chemical ames mutagenicity. *J. Chem. Inf. Model.* **52**, 2840-2847 (2012).
6. Li, X. et al. In silico prediction of chemical acute oral toxicity using multi-classification methods. *J. Chem. Inf. Model.* **54**, 1061-1069 (2014).